

Tuomas Rossi

## **Simulating Electric Field Enhancement in Plasmonic Nanomaterials**

### **School of Science**

Master's thesis submitted in partial fulfillment of the requirements  
for the degree of Master of Science in Technology in the Degree  
Programme in Engineering Physics and Mathematics.

Espoo 5.8.2013

### **Thesis supervisor:**

Prof. Risto Nieminen

### **Thesis advisor:**

Dr. Arto Sakko



**Aalto University**  
School of Science

Author: Tuomas Rossi

Title: Simulating Electric Field Enhancement in Plasmonic Nanomaterials

Date: 5.8.2013

Language: English

Number of pages: 7+59

Department of Applied Physics

Professorship: Engineering Physics

Code: Tfy-105

Supervisor: Prof. Risto Nieminen

Advisor: Dr. Arto Sakko

Localized surface plasmon resonances (LSPRs) are collective excitations of nearly free electrons in plasmonic nanomaterials, such as metal nanoparticles, and they are characterized by charge density oscillation over the whole system. LSPRs lead to strong optical response and enhanced electric near field around the structure, which has been utilized in numerous applications.

This thesis focuses on plasmonic nanomaterials with features of a few nanometers size. The accurate description of the optical properties of such structures necessitates quantum mechanics. The main part of the thesis comprises on implementing computational tools for analyzing optically excited plasmon resonances and the associated electric near field enhancement in these materials. In the thesis, time-dependent density functional theory (TDDFT) and its implementation in GPAW package are used. The methods developed in this thesis are implemented both in real time and in frequency domain and direct comparison between these approaches is presented.

In the literature part of this thesis, the underlying quantum theory of the optical properties of finite nanostructures is reviewed. Additionally, previously published quantum studies on the plasmon resonances are presented. The used methodology is also reviewed, including TDDFT and the projector augmented wave (PAW) method which is employed in GPAW to retain the atomic treatment of material.

The implemented methods are used to study plasmon resonances in a molecular metal atom chain, metal clusters in close contact and a graphene nanoribbon. The obtained results are compared with similar studies from literature. The results show additional details due to small size and the exact atomic background of the studied systems. The effect of different PAW-corrections is also studied. The methods implemented in the thesis are open source, which enables their extensive use also in further studies.

Keywords: plasmonics, LSPR, electric field enhancement, quantum effects, electronic structure calculations, TDDFT, PAW, GPAW

Tekijä: Tuomas Rossi		
Työn nimi: Sähkökentän vahvistumisen simulointi plasmonisissa nanomateriaaleissa		
Päivämäärä: 5.8.2013	Kieli: Englanti	Sivumäärä: 7+59
Teknillisen fysiikan laitos		
Professori: Teknillinen fysiikka		Koodi: Tfy-105
Valvoja: Prof. Risto Nieminen		
Ohjaaja: FT Arto Sakko		
<p>Lokalisoituneet pintaplasmoniresonanssit (LSPR:t) ovat vapaiden elektronien kollektiivisia viritystiloja plasmonisissa nanomateriaaleissa, kuten nanometrien kokoisissa metallipartikkeleissa. LSPR voidaan havainnollistaa koko rakenteen yli olevana varaustiheyden värähtelynä. LSPR aiheuttaa voimakkaan optisen vasteen ja vahvistuneen sähkökentän rakenteen ympärille, mitä on hyödynnetty monissa sovelluksissa.</p> <p>Tämä diplomityö käsittelee plasmonisia nanomateriaaleja, joissa on muutama nanometrin kokoisia rakenteita. Tällaisten rakenteiden optisten ominaisuuksien tarkka mallintaminen vaatii kvanttimekaniikkaa. Diplomityön pääsisältönä on optisesti viritettyjen plasmoniresonanssien ja niiden aiheuttaman sähkökentän vahvistumisen mallintamiseen soveltuvien laskennallisten menetelmien toteuttaminen. Tähän on käytetty ajasta riippuvaa tiheysfunktionaaliteoriaa (TDDFT), jolle on toteutus GPAW-nimisessä ohjelmassa. Diplomityössä kehitetyt menetelmät on toteutettu sekä aika- että taajuusavaruuksissa ja näiden lähestymistapojen tuottamia tuloksia on vertailtu.</p> <p>Diplomityön kirjallisuusosuudessa kuvataan kvanttimekaaninen teoria pienten rakenteiden optisten ominaisuuksien määrittämiseen ja esitellään aiemmin julkaistuja kvanttimekaniikkaan pohjautuvia tutkimuksia plasmoniresonansseista. Työssä kerrataan myös käytetyt menetelmät, kuten TDDFT-teoria ja PAW-menetelmä, jota käytetään GPAW:ssa materiaalien atomistiseen käsittelyyn.</p> <p>Toteutetuilla menetelmillä on tutkittu plasmoniresonansseja molekyylien koluokkaa olevassa metalliatomiketjussa, lähekkäisissä metalliklustereissa ja grafeenihiutaleessa. Saatuja tuloksia on verrattu vastaaviin kirjallisuudessa esitettyihin tuloksiin. Tuloksissa havaitaan yksityiskohtia, jotka aiheutuvat tutkittujen rakenteiden pienestä koosta ja tarkasta atomirakenteesta. Diplomityössä toteutetut menetelmät ovat avointa lähdekoodia, mikä mahdollistaa niiden laajamittaisen käyttämisen myös myöhemmissä tutkimuksissa.</p>		
Avainsanat: plasmoniikka, LSPR, sähkökentän vahvistuminen, kvantti-ilmiöt, elektronirakennelaskut, TDDFT, PAW, GPAW		

## Preface

I implemented the presented methods, made the calculations and wrote this thesis in the Electronic Properties of Materials research group in the Department of Applied Physics, where I started in June 2012 as a summer student doing a special assignment. Since then, I have learned a lot on computational physics and quantum plasmonics, and this thesis puts together part of the knowledge I have gained.

I would like to thank my supervisor Risto Nieminen for introducing me to the field of plasmonics as well as for the continuous support he has given. In addition, I would especially like to thank my instructor Arto Sakko. He has been guiding my work, giving quality feedback and supporting my daily work in all aspects — from practical matters to theoretical considerations. Also, I have had pleasure to present my research and learn more in workshops in Levi, Copenhagen and around Aalto campus. For this opportunity, I am grateful to Risto and our group leader Martti Puska. I am also thankful for computational resources that the local Triton cluster has provided. Furthermore, I would like to thank the people in our research group and in other nearby groups for providing friendly and relaxed working environment.

Otaniemi, 5.8.2013

Tuomas Rossi

# Contents

<b>Abstract</b>	<b>ii</b>
<b>Abstract (in Finnish)</b>	<b>iii</b>
<b>Preface</b>	<b>iv</b>
<b>Notation</b>	<b>vi</b>
<b>1 Introduction</b>	<b>1</b>
<b>2 Optical properties of nanostructures</b>	<b>4</b>
2.1 Electronic structure theory . . . . .	4
2.2 Response to optical light . . . . .	6
2.3 Absorption . . . . .	10
2.4 Localized surface plasmon resonances . . . . .	12
2.5 Electric field enhancement . . . . .	16
<b>3 Time-dependent density functional theory</b>	<b>18</b>
3.1 Ground state: Density functional theory . . . . .	18
3.2 Extending to time dependent case . . . . .	20
3.3 Time propagation method . . . . .	21
3.4 Frequency space methods . . . . .	22
<b>4 Computational methods</b>	<b>27</b>
4.1 Projector augmented wave method . . . . .	27
4.2 Implementation of the field enhancement calculation . . . . .	30
4.2.1 Time propagation method . . . . .	31
4.2.2 Casida method . . . . .	33
<b>5 Model systems and results</b>	<b>37</b>
5.1 Linear metal atom chain . . . . .	37
5.2 Metal cluster dimer . . . . .	41
5.3 Graphene nanoribbon . . . . .	46
<b>6 Conclusions</b>	<b>49</b>
<b>References</b>	<b>51</b>

## Notation

Atomic units, implying  $\hbar = m_e = e = 1/4\pi\epsilon_0 = 1$ , are used throughout the work. For consistency, classical electromagnetism is presented in Gaussian (CGS) units that imply  $1/4\pi\epsilon_0 = 1$ . However, the results in Section 5 are shown in more conventional units ( $\text{\AA}$ , eV) where appropriate.

Many-body operators, such as  $\hat{\mathcal{H}}$ , are denoted by capital letters with a caret  $\hat{\phantom{x}}$  whereas lower case letters are used for single-particle operators, e.g.  $h$ . Within PAW method, smooth pseudo quantities are denoted by a tilde  $\tilde{\phantom{x}}$ .

The lists given below are not exhaustive. Only such symbols and abbreviations are listed that referenced in multiple places of the work. One can also note that some symbols have multiple meanings, but the actual meaning is always evident from the context.

## Symbols

$\delta_{i,j}$	Kronecker delta
$\delta(x)$	delta function
$\theta(x)$	step function
$\mathbf{e}_z$	unit vector in $z$ direction

$\epsilon_0$	vacuum permittivity
$\pi$	pi
$c$	speed of light
$e$	elementary charge
$\hbar$	reduced Planck constant
$m_e$	electron mass

$\eta$	inverse lifetime of an excitation, Lorentzian spectral broadening parameter
$\sigma$	spin, absorption cross-section, Gaussian spectral broadening parameter
$\omega$	(angular) frequency
$\mathbf{r}$	real space coordinate
$t$	time
$\uparrow$	spin up
$\downarrow$	spin down

$\hat{\mathcal{H}}$	many-body Hamiltonian
$\Psi$	many-body wave function
$E$	energy of a many-body state
$\omega_I$	many-body excitation energy
$n$	electron density, complex refractive index

$h$	single-particle hamiltonian
$\psi$	single-particle wave function
$\epsilon$	energy of a single-particle state, relative complex permittivity

$f$	occupation number of a single-particle state
$v$	single-particle potential
$\delta v^{\text{ext}}$	applied single-particle potential
$\mathbf{E}$	electric field
$\chi$	linear density-density response function
$\delta n$	induced electron density
$\delta \rho$	induced charge density
$\delta \phi$	induced electric potential
$\delta \mathbf{E}$	induced electric field
FE	field enhancement
$S$	dipole strength function
$\mu$	dipole moment
$\alpha$	polarizability

## Abbreviations

DFT	density functional theory
EELS	electron energy-loss spectroscopy
ext	external
FE	field enhancement
GGA	generalized gradient approximation
int	interaction
KS	Kohn-Sham
LDA	local density approximation
LSPR	localized surface plasmon resonance
Na	sodium
PAW	projector augmented wave
TDDFT	time-dependent density functional theory
xc	exchange-correlation

# 1 Introduction

Metal nanoparticles have wonderful optical properties that have been fascinating mankind for ages. Since the ancient times, glass staining process has been used to create beautiful ornaments and glass art. The bright colors of stained glass are due to small metal fragments that are embedded in the glass during the glass fabrication process. These tiny particles absorb and scatter certain wavelengths of the visible spectrum of light, giving the color for the stained glass. For example, a specific blend of gold particles yields ruby-red color, and written instructions on producing such color date back to the 17th century [1]. In the middle 19th century, Michael Faraday made scientific experiments on small gold particles and observed the colorful optical properties [2]. Theoretical understanding on the topic was achieved around the same era. The invention of Maxwell’s equations in the 19th century [3], and Gustav Mie’s application of these equations for spherical gold nanoparticles in 1908 [4] provided a theoretical explanation for the ruby-red color of the stained glass. Few years after Mie, Richard Gans generalized Mie’s study to ellipsoidal particle shapes [5, 6].

In modern terms, these optical properties of metal nanoparticles are explained by the collective response of electrons in the particle. The metal atoms’ valence electrons form nearly free electron gas that is confined to the nanoparticle. Impinging electromagnetic field causes the electron plasma to oscillate as a whole in phase with the field. At the characteristic frequency of the system, the electron gas gets into resonance with the external electromagnetic field, which leads to strong resonant absorption and scattering. This collective response is called localized surface plasmon resonance. The resonance frequency is strongly dependent on the size, shape, material and surroundings of the particle as already demonstrated by the work of Mie and Gans. [7–9]

This work focuses on another fascinating property of nanoscale metallic particles: electric near field enhancement. Namely, the coherent charge density oscillation at plasmon resonance leads to strongly enhanced electric near field around the nanoparticle. This field enhancement phenomenon has been a major inspiration for the study of plasmon resonances since the 1970s, when it was observed that Raman scattering signal is significantly enhanced when molecules are placed on a rough metal surface. [10–12] The enhancement in Raman signal is mainly due to strong electric near field of localized surface plasmon resonances that are excited on the rough surface, although also chemical coupling between molecule and surface contributes to the enhanced Raman signal. Since its discovery, surface-enhanced Raman scattering (SERS) has become a valuable spectroscopic tool and even single molecules can be detected with it [13, 14]. In addition, the plasmonic field enhancement phenomenon has also been utilized in other related contexts, e.g. in surface-enhanced absorption and fluorescence. [8]

The electric near field of plasmon resonances enables also novel photonic applications which are not limited by the fundamental diffraction limit. For example, nanoparticle waveguides of sub-wavelength dimensions have been demonstrated [15]. Additionally, interesting physical phenomena can be observed in coupled metal nanoparticles. Plasmon resonances of individual particles hybridize by electrostatic



interaction and form new resonances, providing a classical analogue for bond formation between atoms. [16,17] Interplay between dark and bright plasmon resonances may result in Fano resonances, which in turn can be utilized in highly sensitive sensor applications due to their narrow line width in extinction spectrum. [7] In addition, localized plasmon resonances have shown their usefulness in many other fields, including e.g. photovoltaics [18], photothermal cancer therapy [19] and water purification by solar energy [20].

The technological advances have been enabled by the vast development of experimental fabrication and characterization techniques since the mid-1800s when Faraday performed his experiments. Nowadays, techniques such as electron beam lithography and colloidal synthesis can be used to fabricate nanostructures of well-defined size, shape and composition, which have enabled the utilization of the wide tunability of plasmon resonances. [21] Advanced characterization tools, e.g. atomic force microscopy, scanning tunneling microscopy and electron microscopies, have enabled the observation of the tiny details of the fabricated structures. Localized surface plasmon resonances in these structures can be excited and examined with a number of techniques, including confocal microscopy, near field scanning optical microscopy and electron energy-loss spectroscopy. [9]

The advances in experimental techniques go hand-in-hand with theoretical understanding and modeling. The rapid development of computers during the past decades has enabled accurate numerical simulations of plasmon resonances. Arbitrary nanoparticle geometries and their compounds, which are out of reach of analytical approaches such as the one used by Mie in 1908, can be nowadays studied numerically with e.g. discrete-dipole approximation (DDA) or finite difference time domain (FDTD) methods. The classical electrodynamics based on Maxwell's equations has successfully described plasmon resonances in nanoparticles down to dimensions of tens of nanometers. However, quantum effects need to be taken into account to correctly describe smaller structures. Classical material has abrupt boundaries but the wave nature of electrons leads to spill-out of surface charge in quantum description. Electron tunneling will also significantly modify plasmon resonances of nanoparticles with sub-nanometer separations. In addition, quantum confinement will evidently affect the electronic structure and optical response of nanometer sized particles. [7–9]

To fully take into account these quantum effects, one needs to treat material quantum mechanically from first principles. From several numerical quantum mechanical approaches, time-dependent density functional theory (TDDFT) has become a standard first principles tool for studying localized surface plasmon resonances. Since 1980s, TDDFT has been used to study optical response of small metal clusters, and good agreement with experimental results has been observed. [22–26] In recent studies, the collective plasmonic excitations have been identified also in molecular systems, where optical response is usually interpreted in terms of single electron excitations. [27–33] In addition, a number of studies have demonstrated that quantum effects yield major differences to classical predictions on plasmon resonances. [34–37] Thus, quantum effects cannot be neglected in the study of plasmon resonances, and also schemes for incorporating quantum phenomena in classical sim-

ulations have been developed. [38] In the present work, the focus is on full quantum mechanical treatment of plasmon resonances, and quantum effects are also observed in the systems studied in the work.

Unfortunately, the computational complexity of quantum mechanical calculations is substantially larger than that of classical calculations. However, quantum calculations can be simplified by replacing atomic background with uniform charge density, i.e. with *jellium*. This jellium approximation evidently misses the *ab initio* nature of calculations but allows the study of quantum effects in larger systems. [34–36, 38] However, the jellium approach is expected to be sufficient only for simple metals where nearly free s-electrons dominate the response. For example, in silver and gold, localized d-electrons are known to strongly modify the free electron response [30, 31, 39], and the jellium approximation is not adequate in its simplest form. Additionally, the approximation evidently fails to give correct description of the nanoparticle surface. To retain the *ab initio* nature, a number of studies with atomistic treatment of the ionic background has also been published [27, 29–33, 37, 40–43], and the importance of atomistic treatment is demonstrated also in this work.

All in all, the increased knowledge and interest on plasmon resonances has lead to a new field of science – nanoplasmonics. In the present work, localized surface plasmon resonances in atomically small structures are studied numerically. The quantum mechanical treatment of such small structures is essential and in Section 2 the quantum mechanical description of light-matter interaction is reviewed, with the emphasis on absorption and plasmon resonances. Phenomenological aspects of localized surface plasmon resonances are discussed and previously published quantum mechanical studies on the topic are reviewed in Sections 2.4 and 2.5. The main part of the work comprises of the implementation of tools for analyzing plasmon resonances and the associated field enhancement within general time-dependent density functional theory framework, without limiting to the jellium approximation. The implementation work is done both in time and frequency domains. The underlying time-dependent density functional theory is described in Section 3 and the implemented methods are presented in detail in Section 4. The implemented methods are used to study plasmon resonances in a handful of systems which demonstrate different aspects of plasmon resonances. The obtained results are presented and discussed in Section 5. The thesis is concluded in Section 6.

## 2 Optical properties of nanostructures

Much of the present-day knowledge in the field of materials physics bases on experiments conducted by observing material's response to an external *probe*. However, there is no ultimate probe that would yield all information on the material. Instead, depending on the property of interest, a probe may be e.g. electrons, neutrons or photons, i.e. electromagnetic radiation. The energetics of the probe determines which properties are accessible with it. For example, high energy X-rays excites inner shell electrons of atoms whereas infrared radiation causes vibrational excitations. Visible–ultraviolet light interacts mostly with valence electrons of the matter and can excite single electrons and plasmons, i.e. collective electron excitations. [44, ch. 2]

The focus of the present work is on optically excited localized surface plasmon resonances in nanostructures and, specifically, on their absorption properties and the associated strong electric near field. However, a range of other phenomena, such as emission and scattering, have both theoretical and technological significance in the field of plasmonics even though they are not considered in this work. In addition, it should be noted that e.g. single electron excitations are also present in similar systems in optical energy range although the focus of the work is on collective excitations.

In Sections 2.1 and 2.2, a quantum mechanical description on electrons in nanostructures and on their interaction with optical light are presented. After the theoretical background, a phenomenological and theoretical review of absorption, localized surface plasmon resonances and the associated field enhancement phenomenon is presented in Sections 2.3–2.5.

### 2.1 Electronic structure theory

Quantum mechanical description of electronic properties of materials bases on the many-body Schrödinger equation

$$\hat{\mathcal{H}}\Psi_{\sigma_1\ldots\sigma_N}(\mathbf{r}_1, \ldots, \mathbf{r}_N, t) = i\frac{\partial}{\partial t}\Psi_{\sigma_1\ldots\sigma_N}(\mathbf{r}_1, \ldots, \mathbf{r}_N, t) \quad (2.1)$$

with a Hamiltonian

$$\hat{\mathcal{H}} = \underbrace{-\sum_i \frac{1}{2}\hat{\nabla}_i^2}_{\hat{T}} + \underbrace{\frac{1}{2}\sum_{i\neq j} \frac{1}{|\hat{\mathbf{r}}_i - \hat{\mathbf{r}}_j|}}_{\hat{V}_{\text{int}}} + \underbrace{\sum_i \hat{v}_{\sigma_i}^{\text{ext}}(\mathbf{r}_i, t)}_{\hat{V}_{\text{ext}}}, \quad (2.2)$$

where lower case indices  $i$  and  $j$  refer to the  $N$  identical electrons of the system, and  $\mathbf{r}_i$  and  $\sigma_i$  are  $i$ th electron's spatial and spin degrees of freedom, respectively. [45, ch. 3] Atomic units,  $\hbar = m_e = e = 1/4\pi\epsilon_0 = 1$ , are used throughout this work.

The Hamiltonian  $\hat{\mathcal{H}}$  consists of kinetic energy of electrons, Coulombic electron-electron interactions and external potential,  $\hat{T}$ ,  $\hat{V}_{\text{int}}$  and  $\hat{V}_{\text{ext}}$ , respectively.  $\hat{V}_{\text{ext}}$  is a single particle operator acting on each electron identically. The Hamiltonian includes only electronic degrees of freedom: the nuclei of the material are assumed to be

spatially fixed, which can be justified by their high mass in comparison to that of electrons. This approximation is called the Born-Oppenheimer approximation [46], and e.g. electron-phonon coupling is not captured by it. [45, app. C] Within this simplification, the external potential acting on each electron is given by

$$\hat{v}_\sigma^{\text{ext}}(\mathbf{r}, t) = - \sum_I \frac{Z_I}{|\hat{\mathbf{r}} - \mathbf{R}_I|} + \delta \hat{v}_\sigma^{\text{ext}}(\mathbf{r}, t), \quad (2.3)$$

where  $Z_I$  and  $\mathbf{R}_I$  are electric charge and position of  $I$ th nucleus, respectively. Here  $\delta \hat{v}^{\text{ext}}$  is applied potential, possibly including time-dependence. [45, ch. 3]

The ground state of the system is obtained when  $\delta \hat{v}^{\text{ext}} \equiv 0$ , i.e. the confining external potential is purely the static potential due to nuclei. The resulting Hamiltonian  $\hat{\mathcal{H}}_0$  is time-independent and time can be separated out from the Schrödinger equation, leading to the time-independent Schrödinger equation

$$\hat{\mathcal{H}}_0 \Psi_{\sigma_1 \dots \sigma_N}(\mathbf{r}_1, \dots, \mathbf{r}_N) = E \Psi_{\sigma_1 \dots \sigma_N}(\mathbf{r}_1, \dots, \mathbf{r}_N) \quad (2.4)$$

with the time-independent Hamiltonian

$$\hat{\mathcal{H}}_0 = - \sum_i \frac{1}{2} \hat{\nabla}_i^2 + \frac{1}{2} \sum_{i \neq j} \frac{1}{|\hat{\mathbf{r}}_i - \hat{\mathbf{r}}_j|} + \sum_i \hat{v}_{\sigma_i}^{\text{ext}}(\mathbf{r}_i). \quad (2.5)$$

The time-independent Schrödinger equation defines eigenstates and eigenenergies of the Hamiltonian,  $\Psi_I$  and  $E_I$ , respectively. The ground state  $\Psi_0$  is the state with the lowest energy  $E_0$ . When there is no time-dependent potential, the time evolution of the eigenstates is given by  $\Psi_{\sigma_1 \dots \sigma_N}^I(\mathbf{r}_1, \dots, \mathbf{r}_N, t) = e^{-iE_I t} \Psi_{\sigma_1 \dots \sigma_N}^I(\mathbf{r}_1, \dots, \mathbf{r}_N)$ .

However in practice, the eigenstates of the many-body Hamiltonian are not easily solved for realistic systems — neither analytically or computationally within reasonable time. Even the many-body ground state  $\Psi_0$  is challenging to evaluate, but e.g. variational quantum Monte Carlo techniques can be used for this purpose. [47] Some approximate computational approaches have also been devised. For example, in the Hartree-Fock method it is assumed that the many-body wave function can be presented as a Slater determinant of single particle wave functions, which essentially maps the many-body Schrödinger equation to a non-linear single particle Schrödinger equation. [48, ch. 3] This approach can be further improved in configuration interaction methods, where multiple Slater determinants are used to construct the many-body wave function. [48, ch. 4] Another successful approach is to rigorously reformulate many-body problem in terms of electron density, yielding density functional theory (DFT). [45] In practical DFT implementation, the many-body problem is mapped to effective single particle problem, where the electron interaction is introduced through specific exchange-correlation potential. In this work, this approach is used and density functional theory presented more in detail in Section 3.

## 2.2 Response to optical light

In the study of electrons' interaction with optical light, the interest is in the system's *response* to an applied perturbation. Thus, the system is initially in its ground state  $\Psi_0$ , defined by (2.4) and (2.5), and at some time instance  $t_0$ , an external potential  $\delta\hat{v}^{\text{ext}}(t)$  describing the applied perturbation is switched on. Then one can solve the time evolution of the initial state from the time-dependent Schrödinger equation (2.1) to obtain  $\Psi(t)$  and the system's response.

The electromagnetic field can be described fully quantum mechanically in terms of photons, i.e. quanta of the field. However, for the present purposes, it suffices to describe the field classically in terms of its electric and magnetic field components,  $\mathbf{E}(\mathbf{r}, t)$  and  $\mathbf{B}(\mathbf{r}, t)$ , or in terms of the vector and scalar potentials,  $\mathbf{A}(\mathbf{r}, t)$  and  $\phi(\mathbf{r}, t)$ . For nanostructures much smaller than the wavelength of the perturbing field, the spatial variation of the field is negligible over the system, so the field can be assumed to be spatially constant. Within this so called dipole approximation, the classical electromagnetic field can be described through spin-independent potential

$$\delta\hat{v}_\sigma^{\text{ext}}(\mathbf{r}, t) = \hat{\mathbf{r}} \cdot \mathbf{E}(t), \quad (2.6)$$

by invoking the requirement of local gauge invariance. [49, ch. 5] Here  $\mathbf{E}(t)$  is the electric part of the electromagnetic field, including only time dependence. For a single-mode field, the time dependence is of form  $\mathbf{E}(t) = \mathbf{E}_0 \cos(\omega t)\theta(t)$  where the step function emphasizes the switch-on of the field at time  $t_0 = 0$ .

In addition to its rigorous derivation, the coupling operator (2.6) can be justified in a simpler way. First, the magnetic field component of the electromagnetic field is not included since it is relatively weaker than the electric field component. Secondly, the assumed large wavelength, i.e. small frequency, corresponds to the quasi-static description of the electromagnetic field, and (2.6) is the same potential that describes coupling between static electric field and the negatively charged electrons.

The electrons' response to the perturbing field is seen as variations in the electron density. The density operator is defined as  $\hat{n}_\sigma(\mathbf{r}) = \sum_i \delta_{\sigma, \sigma_i} \delta(\mathbf{r} - \mathbf{r}_i)$ . Thus, the time evolution of the density is given by

$$\begin{aligned} n_\sigma(\mathbf{r}, t) &= \langle \Psi(t) | \hat{n}_\sigma(\mathbf{r}) | \Psi(t) \rangle \\ &= \sum_{\sigma_1 \dots \sigma_N} \int d\mathbf{r}'_1 \dots \int d\mathbf{r}'_N \sum_i \delta_{\sigma, \sigma_i} \delta(\mathbf{r} - \mathbf{r}'_i) |\Psi_{\sigma_1 \dots \sigma_N}(\mathbf{r}'_1, \dots, \mathbf{r}'_N, t)|^2, \end{aligned} \quad (2.7)$$

and the ground state density is correspondingly  $n_\sigma^0(\mathbf{r}) = \langle \Psi_0 | \hat{n}_\sigma(\mathbf{r}) | \Psi_0 \rangle$ . The total charge density is given by

$$\rho(\mathbf{r}, t) = - \sum_\sigma n_\sigma(\mathbf{r}, t) + \sum_I Z_I \delta(\mathbf{r} - \mathbf{R}_I), \quad (2.8)$$

where  $Z_I \delta(\mathbf{r} - \mathbf{R}_I)$  is charge density of  $I$ th nucleus.

The applied perturbation induces a change to the electron density,  $\delta n_\sigma(\mathbf{r}, t) = n_\sigma(\mathbf{r}, t) - n_\sigma^0(\mathbf{r})$ . This can be expressed as a series in the perturbation

$$\delta n_\sigma(\mathbf{r}, t) = \int_{-\infty}^{\infty} dt' \sum_\tau \int d\mathbf{r}' \chi_{\sigma, \tau}(\mathbf{r}, \mathbf{r}', t - t') \delta v_\tau^{\text{ext}}(\mathbf{r}', t') + O((\delta v^{\text{ext}})^2), \quad (2.9)$$

where  $\chi_{\sigma,\tau}(\mathbf{r}, \mathbf{r}', t - t')$  is the linear density-density response function. [44, ch. 4] In the present description, the nuclei are assumed to be fixed in space, whence nuclear vibration effects are neglected and the total induced charge density is given purely by the electron contribution, i.e.  $\delta\rho(\mathbf{r}, t) = -\sum_{\sigma} \delta n_{\sigma}(\mathbf{r}, t)$ .

The series expression (2.9) is reasonable if the perturbing potential  $\delta v^{\text{ext}}$  is of sufficiently small magnitude. In this work, the focus is on linear response, i.e. the perturbation  $\delta v^{\text{ext}}$  is so weak that higher order terms can be neglected,  $O(\delta v^2) \approx 0$ , and the response function  $\chi$  describes the full density response. However, higher order terms are required to describe nonlinear effects, which can be experimentally observed by e.g. intense laser fields. [44, ch. 18]

The density-density response function can be expressed in terms of the eigenstates of the ground state Hamiltonian  $\hat{\mathcal{H}}_0$ . By invoking the time-dependent perturbation theory, one obtains

$$\chi_{\sigma,\tau}(\mathbf{r}, \mathbf{r}', t - t') = -i\theta(t - t') \langle \Psi_0 | [\hat{n}_{\sigma}^{\text{H}}(\mathbf{r}, t), \hat{n}_{\tau}^{\text{H}}(\mathbf{r}', t')] | \Psi_0 \rangle, \quad (2.10)$$

where  $\hat{n}_{\sigma}^{\text{H}}(\mathbf{r}, t) = e^{i\hat{\mathcal{H}}_0 t} \hat{n}_{\sigma}(\mathbf{r}) e^{-i\hat{\mathcal{H}}_0 t}$  is the density operator in the Heisenberg picture. [50, p. 173] By opening the commutator and inserting completeness relation  $\sum_I |\Psi_I\rangle \langle \Psi_I| = \hat{I}$  between the density operators, this can be re-expressed as

$$\begin{aligned} \chi_{\sigma,\tau}(\mathbf{r}, \mathbf{r}', t - t') = -i\theta(t - t') \sum_{I \neq 0} & \left( \langle \Psi_0 | \hat{n}_{\sigma}(\mathbf{r}) | \Psi_I \rangle \langle \Psi_I | \hat{n}_{\tau}(\mathbf{r}') | \Psi_0 \rangle e^{-i(E_I - E_0)(t - t')} \right. \\ & \left. - \langle \Psi_0 | \hat{n}_{\tau}(\mathbf{r}') | \Psi_I \rangle \langle \Psi_I | \hat{n}_{\sigma}(\mathbf{r}) | \Psi_0 \rangle e^{i(E_I - E_0)(t - t')} \right), \end{aligned} \quad (2.11)$$

since the  $I = 0$  terms cancel each other in the sum. [44, p. 73] Thus, the knowledge of the matrix elements  $\langle \Psi_0 | \hat{n}_{\sigma}(\mathbf{r}) | \Psi_I \rangle$  provides access to the density-density response function and all properties derivable from it, e.g. the induced density (2.9).

The induced density is itself physically measurable quantity, but integral quantities are often defined to capture the global response of the system. For example, the time-dependent electric dipole moment is defined as

$$\boldsymbol{\mu}(t) = -\sum_{\sigma} \int d\mathbf{r} \mathbf{r} n_{\sigma}(\mathbf{r}, t) = -\langle \Psi(t) | \sum_i \hat{\mathbf{r}}_i | \Psi(t) \rangle, \quad (2.12)$$

where the minus sign comes from the negative charge of the electrons as the dipole moment is defined for the charge density. [44, ch. 7] To describe the response of the system, induced dipole moment is defined analogously to the induced density, i.e.  $\delta\boldsymbol{\mu}(t) = \boldsymbol{\mu}(t) - \boldsymbol{\mu}_0 = -\sum_{\sigma} \int d\mathbf{r} \mathbf{r} \delta n_{\sigma}(\mathbf{r}, t)$ . One should note that as the nuclei are assumed to be fixed in space, the induced electric dipole moment is equivalent to the induced dipole moment, which is defined analogously for the total charge density (2.8).

In the linear response regime, a major quantity is dynamical polarizability  $\boldsymbol{\alpha}(t)$ , which describes the time-dependent response of the system's dipole moment to the perturbation. Polarizability is a tensor quantity whose elements are defined as follows. If the perturbing electric field is polarized in the  $z$  direction, i.e.  $\mathbf{E}(t) = \mathbf{e}_z E_z(t)$

and  $\delta\hat{v}^{\text{ext}}(\mathbf{r}, t) = \hat{z}E_z(t)$  in (2.6), then the  $x$  component of the induced dipole moment can be expressed as a series of the perturbing field as

$$\delta\mu_x(t) = \int_{-\infty}^{\infty} dt' \alpha_{xz}(t-t')E_z(t') + O(E_z^2), \quad (2.13)$$

where the first order term defines the  $xz$  component of polarizability,  $\alpha_{xz}$ , and the higher order terms are neglected in linear response theory. [51] Usually, one can expect the system's response to be strongest in the same direction as the perturbing field, in which case the diagonal elements of the polarizability dominate.

So far the response properties have been described in time domain. However, it is useful to reformulate the response properties in frequency space as experiments are usually performed as a function of frequency. For example, light of fixed frequency (i.e. fixed energy) can be used to probe system's response at this frequency. Time and frequency spaces are related through standard Fourier transforms: for a general function  $f$

$$f(\omega) = \int_{-\infty}^{\infty} dt f(t)e^{i\omega t}, \quad f(t) = \frac{1}{2\pi} \int_{-\infty}^{\infty} d\omega f(\omega)e^{-i\omega t}. \quad (2.14)$$

By the convolution theorem of the Fourier transformation, the time-convolution integrals in (2.9) and (2.13) simplify to products in frequency space. Thus in frequency space,

$$\delta n_{\sigma}(\mathbf{r}, \omega) = \sum_{\tau} \int d\mathbf{r}' \chi_{\sigma,\tau}(\mathbf{r}, \mathbf{r}', \omega) \delta v_{\tau}^{\text{ext}}(\mathbf{r}', \omega) \quad (2.15)$$

and

$$\delta\mu_x(\omega) = \alpha_{xz}(\omega)E_z(\omega), \quad (2.16)$$

up to linear order. The density-density response function (2.11) can be expressed in frequency space by using the Fourier transformation of the step function,

$$\theta(t-t') = -\frac{1}{2\pi i} \int_{-\infty}^{\infty} d\omega \frac{1}{\omega + i\eta} e^{-i\omega(t-t')}, \quad (2.17)$$

where  $\eta \rightarrow 0^+$  is a positive infinitesimal. [50, p. 72] This leads to the Lehmann representation of the density-density response function

$$\chi_{\sigma,\tau}(\mathbf{r}, \mathbf{r}', \omega) = \sum_{I \neq 0} \left( \frac{\langle \Psi_0 | \hat{n}_{\sigma}(\mathbf{r}) | \Psi_I \rangle \langle \Psi_I | \hat{n}_{\tau}(\mathbf{r}') | \Psi_0 \rangle}{\omega - \omega_I + i\eta} - \frac{\langle \Psi_0 | \hat{n}_{\tau}(\mathbf{r}') | \Psi_I \rangle \langle \Psi_I | \hat{n}_{\sigma}(\mathbf{r}) | \Psi_0 \rangle}{\omega + \omega_I + i\eta} \right), \quad (2.18)$$

where  $\omega_I = E_I - E_0$  are excitation energies of the many-body system. [44, p. 73] The Lehmann representation is an important result which is also needed later in this work, see Sections 3.4 and 4.2.2.

In frequency space, the polarizability can be conveniently expressed in terms of the induced density (2.15) or the linear response function in the Lehmann representation (2.18). For  $z$  polarized electric field,  $\delta\hat{v}^{\text{ext}}(\mathbf{r}, \omega) = \hat{z}E_z(\omega)$ , and the

polarizability (2.16) is given by following forms

$$\begin{aligned}
\alpha_{xz}(\omega) &= \frac{\delta\mu_x(\omega)}{E_z(\omega)} = -\frac{1}{E_z(\omega)} \sum_{\sigma} \int d\mathbf{r} x \delta n_{\sigma}^z(\mathbf{r}, \omega) \\
&= -\sum_{\sigma, \tau} \int d\mathbf{r} \int d\mathbf{r}' x \chi_{\sigma, \tau}(\mathbf{r}, \mathbf{r}', \omega) z' \\
&= -\sum_{I \neq 0} \left( \frac{\langle \Psi_0 | \hat{x} | \Psi_I \rangle \langle \Psi_I | \hat{z} | \Psi_0 \rangle}{\omega - \omega_I + i\eta} - \frac{\langle \Psi_0 | \hat{z} | \Psi_I \rangle \langle \Psi_I | \hat{x} | \Psi_0 \rangle}{\omega + \omega_I + i\eta} \right),
\end{aligned} \tag{2.19}$$

where the last expression simplifies in the limit  $\eta \rightarrow 0^+$  to

$$\alpha_{xz}(\omega) = \sum_{I \neq 0} \frac{2\omega_I}{\omega_I^2 - \omega^2} \langle \Psi_0 | \hat{x} | \Psi_I \rangle \langle \Psi_I | \hat{z} | \Psi_0 \rangle, \tag{2.20}$$

since  $\langle \Psi_0 | \hat{x} | \Psi_I \rangle \langle \Psi_I | \hat{z} | \Psi_0 \rangle = \langle \Psi_0 | \hat{z} | \Psi_I \rangle \langle \Psi_I | \hat{x} | \Psi_0 \rangle$  [51].

As the physically relevant response functions are causal in time, i.e. the future events cannot affect the past, as is emphasized by  $\theta(t - t')$  in (2.10), the real and imaginary parts of response functions in frequency domain are related through the Kramers-Kronig relations. [44, p. 44] In general, for a response function  $\chi$  the Kramers-Kronig relations state that

$$\text{Re}[\chi(\omega)] = -\frac{1}{\pi} \mathcal{P} \int_{-\infty}^{\infty} d\omega' \frac{\text{Im}[\chi(\omega')]}{\omega - \omega'} \tag{2.21a}$$

and

$$\text{Im}[\chi(\omega)] = \frac{1}{\pi} \mathcal{P} \int_{-\infty}^{\infty} d\omega' \frac{\text{Re}[\chi(\omega')]}{\omega - \omega'}, \tag{2.21b}$$

where  $\mathcal{P} \int_{-\infty}^{\infty} d\omega' = \lim_{\varepsilon \rightarrow 0^+} \left( \int_{-\infty}^{\omega - \varepsilon} d\omega' + \int_{\omega + \varepsilon}^{\infty} d\omega' \right)$  is a principal value integral. In the present case, the Kramers-Kronig relations hold for the density-density response function  $\chi_{\sigma, \tau}(\mathbf{r}, \mathbf{r}', \omega)$  as well as for the induced density  $\delta n_{\sigma}(\mathbf{r}, \omega)$  and the polarizability  $\alpha(\omega)$ .

The linear response of a nanostructure to a perturbing optical light is formally solved here but the presented formalism is not directly feasible for studying realistic systems. Namely, the sum-over-states expressions (2.18) and (2.19) cannot be directly evaluated as the many-body wave functions  $\Psi_I$  are not easily solved as discussed in Section 2.1. However, e.g. the configuration interaction methods can be used to calculate response properties [42]. Response function is also related to Green's functions, which are utilized in e.g. GW calculations. [52] In addition, time-dependent extensions of the previously mentioned approaches, i.e. Hartree-Fock and density functional theory, can be used to calculate optical response of nanostructures. [44, 53] Time-dependent density functional theory (TDDFT) is used in this work and it is presented both in time and frequency domains in Section 3.



## 2.3 Absorption

A nanostructure can absorb energy of the light focused on it. The imaginary part of the dynamical polarizability  $\alpha(\omega)$  can be associated with the absorption cross-section of the nanostructure. To construct a proper definition for the absorption cross-section, a brief summary of absorption in macroscopic scale is first given. Gaussian units are used throughout this section.

The classical description of electromagnetic radiation bases on Maxwell's equations. The Maxwell's equations yield a wave equation for the propagating electromagnetic field. In a uniform dielectric medium, a general solution for the electric field part of the electromagnetic field is obtained from the wave equation as

$$\mathbf{E}(\mathbf{r}, t) = \mathbf{E}_0 e^{i(\mathbf{k} \cdot \mathbf{r} - \omega t)}, \quad (2.22)$$

where  $\mathbf{k}$  and  $\omega$  are the wave vector and (angular) frequency of the electromagnetic field. They are related through dispersion relation

$$k = |\mathbf{k}| = \frac{n(\omega)}{c} \omega, \quad (2.23)$$

where  $n(\omega)$  is the refractive index of the medium. [54, ch. 5.8]

The refractive index is connected to the dielectric function as  $\epsilon(\omega) = (n(\omega))^2$ , and the dielectric function  $\epsilon(\omega)$  is defined through relation

$$\mathbf{P}(\omega) = \frac{1}{4\pi} (\epsilon(\omega) - 1) \mathbf{E}(\omega), \quad (2.24)$$

where  $\mathbf{P}(\omega)$  is the polarization density. So, the dielectric function describes the macroscopic linear response of the medium to the external electric field. In general,  $\epsilon(\omega)$  is a complex quantity,  $\epsilon(\omega) = \epsilon_1(\omega) + i\epsilon_2(\omega)$ , whose real and imaginary parts,  $\epsilon_1$  and  $\epsilon_2$ , are related through the Kramers-Kronig relations (2.21). Similarly, the refractive index is complex, expanded as  $n(\omega) = n_1(\omega) + in_2(\omega)$ . The real and complex parts of the dielectric function and refractive index are related through

$$\epsilon_1 = n_1^2 - n_2^2 \quad \text{and} \quad \epsilon_2 = 2n_1 n_2 \quad (2.25)$$

by the relation  $\epsilon = n^2$ . [55, ch. 27]

The imaginary part of the refractive index or dielectric function can be associated with absorption. To see this, consider an electromagnetic field propagating in  $z$  direction, i.e.  $\mathbf{k} = \mathbf{e}_z k$ . Then (2.22) can be written as

$$\mathbf{E}(\mathbf{r}, t) = \mathbf{E}_0 e^{i\frac{\omega}{c}(n_1(\omega)z - ct)} e^{-\frac{\omega}{c}n_2(\omega)z}. \quad (2.26)$$

Thus, the field intensity  $I = |\mathbf{E}|^2$  decays exponentially,

$$I(z) = |\mathbf{E}_0|^2 e^{-2\frac{\omega}{c}n_2(\omega)z}, \quad (2.27)$$

where the exponent provides following definition for the absorption coefficient:

$$K(\omega) = \frac{2\omega}{c} n_2(\omega) = \frac{\omega}{c} \frac{\epsilon_2(\omega)}{n_1(\omega)}. \quad (2.28)$$

The last equality in (2.28) results from (2.25). [54, ch. 5.8]

To relate the macroscopic attenuation of the electric field to the absorption of the microscopic constituents of the sample material, consider a medium consisting of isotropic assemblage of identical molecules (or nanostructures) with isotropic polarizability  $\alpha(\omega)$ . Then the macroscopic dielectric function is given by the Clausius-Mossotti relation

$$\frac{\epsilon(\omega) - 1}{\epsilon(\omega) + 2} = \frac{4\pi}{3} \frac{N}{V} \alpha(\omega), \quad (2.29)$$

where  $N/V$  is the number density of the molecules. [55, ch. 27]

If the molecules are scattered sparsely, i.e. they have only minor contribution to large scale properties, then by (2.24) the macroscopic dielectric function is  $\epsilon(\omega) \approx 1$ , i.e.  $\epsilon_1(\omega) \approx 1$  and  $\epsilon_2(\omega) \approx 0$ . Correspondingly, the refractive index is  $n(\omega) \approx 1 + 0i$ . In this case, Clausius-Mossotti relation (2.29) simplifies to  $\epsilon(\omega) - 1 = 4\pi \frac{N}{V} \alpha(\omega)$ . Consequently, with these assumptions the absorption coefficient (2.28) reads

$$K(\omega) = \frac{N}{V} \underbrace{\frac{4\pi\omega}{c} \text{Im}[\alpha(\omega)]}_{\sigma(\omega)}, \quad (2.30)$$

which defines the molecular absorption cross-section  $\sigma(\omega)$ .

Usually the molecular polarizability is not isotropic, and the different orientations of the molecule need to be considered separately. For the general polarizability tensor  $\boldsymbol{\alpha}(\omega)$ , the absorption cross-section is defined for each orientation, e.g.

$$\sigma_{zz}(\omega) = \frac{4\pi\omega}{c} \text{Im}[\alpha_{zz}(\omega)]. \quad (2.31)$$

However, in practical experiments on randomly oriented molecules, different orientations should be averaged out, yielding the experimental cross section  $\sigma(\omega) = \frac{1}{3}(\sigma_{xx}(\omega) + \sigma_{yy}(\omega) + \sigma_{zz}(\omega))$ . [44, ch. 3]

Another quantity describing the molecular absorption is the dipole strength function  $S_z(\omega)$ , which is obtained by scaling the absorption cross-section as

$$S_z(\omega) = \frac{c}{2\pi^2} \sigma_{zz}(\omega) = \frac{2\omega}{\pi} \text{Im}[\alpha_{zz}(\omega)]. \quad (2.32)$$

The dipole strength function satisfies the sum rule  $\int_0^\infty d\omega S_z(\omega) = N_e$ , where  $N_e$  is the number of electrons in the molecule. [44, ch. 3]

All in all, the absorption cross-section of molecules is obtained from the dynamical polarizability, which can be formally solved from quantum mechanics as described in Section 2.2. Experimentally absorption coefficient can be determined by measuring the attenuation of the field intensity as the electromagnetic field traverses through the sample, c.f. (2.27). However, practical aspects of the actual experiments are not pursued further in this work. [56]

## 2.4 Localized surface plasmon resonances

Localized surface plasmon resonances (LSPRs) are collective electron excitations in metal nanoparticles. LSPR is characterized by coherent charge density oscillation over the whole particle. The resonance condition is established at system specific frequencies, which are determined by the size, shape, material and surroundings of the particle. Thus, by using advanced fabrication techniques, the plasmon resonance can be tuned to frequency that is optimal for the application at hand. This is a key property for enabling utilization of plasmon resonances in numerous contexts, c.f. Section 1.

Localized surface plasmon resonance is illustrated in Figure 2.1. A typical polarizability spectrum for a simple system with single plasmon resonance is also shown. Additionally, frequency representations of induced densities are presented below, at, and above the resonance frequency  $\omega_p$ . Below  $\omega_p$ , electrons oscillate in phase with the field, i.e. the response is dominated by the real part. At  $\omega_p$ , strong resonant charge density oscillation is characterized by imaginary frequency response, i.e. electrons oscillate coherently with  $\pi/2$  phase lag in comparison to the perturbing field. Above  $\omega_p$ , the perturbing field oscillates too fast for electrons in the system to respond.

In general, a nanoparticle can support various plasmon modes at different frequencies, and perturbing the system at one of these characteristic frequencies can excite the localized surface plasmon. [57] In this work, the focus is on plasmon modes that are excitable by light. For nanoscale particles, this means that they are excitable by dipolar perturbation, c.f. Section 2.2. Hence, the associated plasmonic

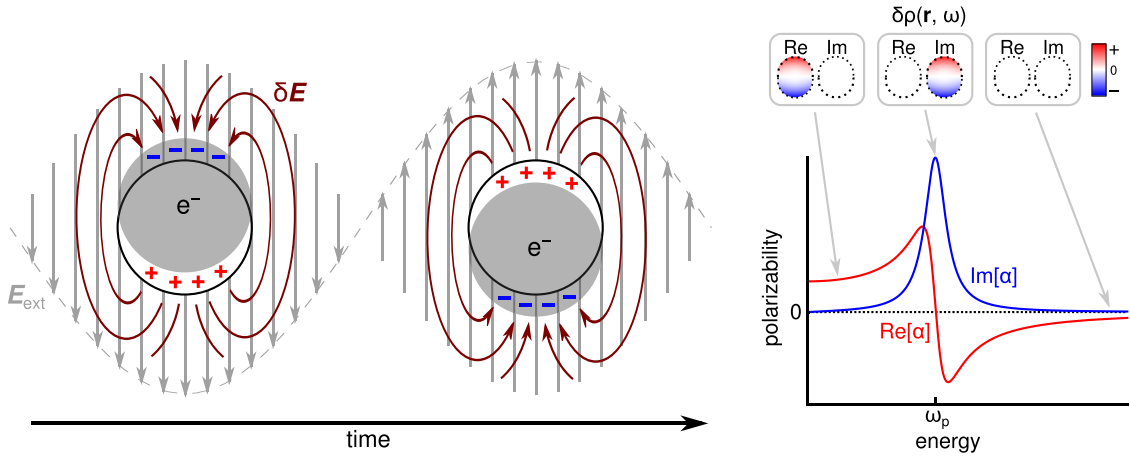


**Figure 2.1.** Illustration of localized surface plasmon resonance. Left: response in time domain: charge density oscillation and the associated induced electric near field. Right: response in frequency domain: polarizability and induced densities at specific frequencies. Note that due to artistic reasons, following details are not included in the figure: first, the dipole approximation is fulfilled only for clusters whose diameter is much smaller than the wavelength of external electromagnetic field, and second, at resonance the electron density oscillation lags in phase by  $\pi/2$ . See text for detailed discussion.

charge density oscillation has to have finite dipole moment in order to be observed optically. In addition, the larger the dipole moment is, the stronger the response will be, c.f. absorption in (2.32) and (2.19). These light induced plasmon modes are usually referred as *bright* modes whereas optically inactive modes are called *dark* modes. Even though dark modes cannot be observed by optical means, they can be excited with different probes. For example, electron beam can be used to excite dark multipolar modes in addition to the bright dipolar modes, as is done in electron energy-loss spectroscopy (EELS). [58, 59]

Nevertheless, "dark" plasmon modes can also be probed with light in larger structures where dipole approximation is no more valid, i.e. it takes finite time from light to traverse through the structure, leading to phase retardation of the electromagnetic field. [57, 60] However, for such large clusters, light does not excite free plasmons, but rather plasmon polaritons, which are plasmons coupled to the outer electromagnetic field. The plasmon polaritons exhibit increased radiation damping compared to the free plasmons, which leads to shift in resonance frequencies. [57] Nonetheless, for atomically small structures considered in this work, the quasi-static description of electromagnetic field is valid and plasmon polaritons coincide with free plasmons.

Experimentally, plasmonic nanostructures are fabricated using various methods. Lithographic techniques allow fabrication of well-controlled geometries. Feature sizes accessible with optical lithography are limited by the diffraction of light, but nanoscale feature sizes can be reached with focused ion beam and electron beam lithography [61]. Bottom-up fabrication methods, such as thermal evaporation and chemical synthesis techniques, can be used to fabricate nanoparticles of various sizes and shapes, and synthesis of few-nanometer sized silver clusters has been demonstrated [62, 63]. Furthermore, electron microscope can be used to move these tiny clusters to form e.g. cluster dimer [64]. Alternatively, synthesized nanoparticles can be organized in specific shapes by self-assembly. [9, 21] In the extreme case of single atoms, a precise control of atom positions has been demonstrated with scanning tunneling microscopy [65–67].

Fabricated nanostructure can be imaged by using standard techniques, e.g. atomic force microscopy (AFM), scanning tunneling microscopy (STM) and different electron microscopies (SEM, TEM, STEM). The plasmon resonances can be excited with light or electron beams. Excitation spectra can be measured with optical techniques, such as confocal microscopy, dark-field microscopy and photodepletion measurements, or with electron probes, e.g. cathodoluminescence (CL) and EELS. [9, 21, 68] In addition to the fact that dark modes can be excited with electron impact, another advantage of electron beams is that they can be sharply focused, which allow obtaining real space picture of plasmon modes at sub-nanometer resolution. [9, 69–71] The same is not possible with conventional optical techniques that are limited by the diffraction of light. However, scanning near-field optical microscope (SNOM) can be used for mapping electric near field of plasmon resonances in real space. [9]

Theoretically, localized surface plasmon resonances are well described with classical electrodynamics based on Maxwell's equations, where material's response is described by its dielectric function  $\epsilon(\omega)$ . For example, the finite difference time do-

main (FDTD) method is a popular way to solve Maxwell's equations numerically for arbitrary geometries. [72] Many theoretical studies have been conducted with the aim of e.g. tuning plasmon resonances to desired frequency range and finding geometries that yield particularly strong and sharply localized near field. Generally, good agreement between classical calculations and experimental measurements has been observed. [7–9]

A wealth of theoretical understanding has been achieved with so called plasmon hybridization model, which describes plasmon modes of complex structures as a mixture of plasmon modes of simpler subsystems. [16,17] For example, in a case of metal cluster dimer, electrostatic interaction between plasmons of individual clusters yields new hybridized bonding and anti-bonding plasmon modes to the whole complex, in analogy to molecular bonding. Avoided crossing between different hybridized plasmon modes can also be observed in symmetry broken systems. [17] Hybridization of plasmon modes of different multipolar order may also render dark plasmon modes optically active. [17, 73] Hybridization model is also important for understanding Fano resonances, which are observed when sharp dark plasmon mode overlaps in energy with broad bright plasmon mode. [7] For example, in an asymmetric dolmen structure formed by three metal particles, dipolar plasmon modes in each particle can interact to form quadrupolar mode over the whole dolmen, resulting in a dip in excitation spectrum that is characteristic to Fano resonances. [74]

Although Maxwell's equations have been successfully applied for describing plasmons, they fail to reproduce quantum effects due to their classical basis. For clusters smaller than around 10 nanometers in diameter, the material's description in terms of dielectric function  $\epsilon(\omega)$  becomes insufficient. Effective cluster size dependent dielectric function can be devised to take into account the increasing surface-to-volume ratio but quantum mechanical description is needed for fully describing the response of small particles. [8,57] Recently, quantum effects in plasmon resonances have also been experimentally observed [63,64,75].

When the particle sizes approach molecular dimensions, electronic states become discrete due to quantum confinement. In this size regime, electronic excitations are conventionally described as single-particle transitions between system's eigenstates. However, quantum mechanical time-dependent density functional theory (TDDFT) studies have shown that in molecular metal clusters some excitations exhibit plasmonic nature, i.e. they are interpretable as charge density oscillations of confined electron gas. This characterization has been reasoned by the strengthening of the excitations with increasing cluster size as well as by visual inspection of the associated density oscillations. [27–31] In addition, an approach based on scaling the electron-electron interaction in a TDDFT calculation has been proposed for identifying plasmonic excitations from ordinary single-particle excitations. [32] This method gives plasmonic characterization in accordance with the visual inspection of the charge density oscillations. In these studies, a linear metal atom chain has been used as a simplest molecular model system supporting plasmons [28–33]. Also in this work, the atom chain is used as model system, see Section 5.1.

Quantum effects in plasmon resonances have also been studied in larger, but still nanoscale, structures. The jellium approximation, i.e. replacing the atomic

background with uniform background charge density, may be employed for studying plasmon resonances since the nearly free electron gas is reproduced in jellium. The jellium approximation allows quantum mechanical study of larger systems and excellent agreement between quantum calculations and classical theory has been demonstrated for plasmon resonance frequencies in metallic nanoshells. [34] However, quantum effects have also been observed. Plasmon resonances in jellium nanorods show spectral tunability that is in accordance with classical predictions, but quantum calculations show strongly modified electric near field close to the nanorod surface. This is due to spill-out of surface charge which is not captured by classical calculations where material has abrupt boundaries. [36] Similar effect is quantum mechanical tunneling which strongly modifies plasmon resonances in coupled metal clusters in close contact, leading to e.g. charge transfer plasmon modes, which are not present in classical calculations of non-overlapping dimers. [35] In this work, similar quantum effects are observed in molecular clusters, see Section 5.2.

The jellium approximation can be used to realize quantum effects but it is not out of limitations. In the jellium approach, different materials are described with semi-empirical electron density parameter, which is inevitably a major simplification for describing the atomic nature of material. For example, for small molecular systems studied in this work, it is essential to keep the atomic treatment of ionic background. Also in larger systems, the jellium approximation is not expected to give precise description of surface effects in cases where the atomic roughness of the surface is relevant. The full atomic treatment is also required to correctly describe the localized d-electrons in noble metals. There the d-electrons are energetically close to the nearly free s-electrons that yield the plasmon resonances, and d-electrons may screen plasmon resonances [30, 31, 39]. Due to these limitations, atomically treated ionic background has been used to study e.g. atom planes [76], silver nanorods [41] and silver clusters [37], in addition to the atom chain studies mentioned previously. Also in this work, implementation work and calculations are performed for atomistically treated systems.

The atomistic treatment of ionic background is also essential for non-metallic systems. In fact, localized plasmon resonances can also be observed in small graphene flakes, and enhanced electric near field has been predicted with quantum-mechanical tight-binding [43] and semi-empirical Hartree-Fock based methods [42]. In Section 5.3, the methods implemented in this work are used for studying field enhancement in graphene nanoribbon.

Although the focus of the present work is in the localized surface plasmon resonances in nanoparticles, it should be mentioned that similar collective electron oscillations takes place in extended geometries. Free electron gas in metals support longitudinal charge density oscillations in the bulk and confined on the surface, and quanta of these oscillations are called volume and surface plasmons, respectively. The free electron gas behavior in metals explains also good optical reflectivity of metals. However, interband transitions in noble metals modify the free electron behavior, giving e.g. gold its unique color. [54, 77]

The volume and surface plasmon modes are observed in EELS spectrum, but they are not directly excitable with light. However, surface plasmons can be cou-

pled to radiative light by using gratings or prisms. [77] Surface plasmons and LSPRs are strongly related concepts, and as the name suggests, localized surface plasmon resonance can be interpreted as a surface plasmon localized to the small nanoparticle. Like LSPRs, surface plasmons essentially confine light into subwavelength dimensions, and one of their promising applications is in realizing photonic devices below the diffraction limit. [39, 78] A transition from surface plasmons to localized plasmons is present on surfaces with increasing roughness. On a surface with minor roughness, surface plasmons are present, whereas on rougher surfaces the description in terms of localized surface plasmon resonance at each bump's sharp tip is more applicable. However, in the intermediate regime these concepts overlap, as is also the case when the surface is so dense of the sharp tips that localized plasmon in adjacent tips couple strongly. [79]

However, surface plasmons differ from their localized counterparts in their interaction with (self-generated) electromagnetic field. In extended domains such as surfaces, separation between plasmons and plasmon polaritons is necessary, whereas in small clusters quasi-static limit is generally valid and localized plasmon and plasmon polariton are essentially the same concept, as discussed above. However, surfaces can support plasma oscillations with variable phase velocities. Surface plasmon corresponds to low velocities, i.e. non-propagating limit, and its interaction with electromagnetic field is well approximated in quasi-static, i.e. nonretarded, limit. For phase velocities which are comparable with speed of light, retardation effects are present, and in this regime plasma oscillations are plasmon polaritons, i.e. propagating charge density waves. [39]

## 2.5 Electric field enhancement

The coherent oscillation of the charge density at plasmon resonance in a nanostructure induces electric near field around the structure, c.f. Figure 2.1 in Section 2.4. Since the density oscillation is intense at plasmon resonance, the induced electric field is in many cases much stronger than the external perturbing electric field. This electric near field enhancement phenomenon has been utilized in many applications as described in Section 1. Quantum mechanical studies on field enhancement have shown significant deviations from the classical predictions due to spill-out of surface charge and electron tunneling, c.f. Section 2.4, and such effects are observed also in this work, see Section 5.

The charge density oscillations are described by time-dependent induced charge density  $\delta\rho(\mathbf{r}, t) = -\sum_{\sigma} \delta n_{\sigma}(\mathbf{r}, t)$ , c.f. (2.9), which includes only electronic contribution as nuclei are assumed to be fixed in space. For the induced density, associated induced electric potential, i.e. Hartree potential, can be defined as

$$\delta\phi(\mathbf{r}, t) = \int d\mathbf{r}' \frac{\delta\rho(\mathbf{r}', t)}{|\mathbf{r} - \mathbf{r}'|}. \quad (2.33)$$

Then, in quasi-static limit, the classical induced electric field is obtained from the potential as  $\delta\mathbf{E}(\mathbf{r}, t) = -\nabla\delta\phi(\mathbf{r}, t)$ . The quasi-static approximation should give a good description for the induced electric field near the nanostructure that is of

interest in this work. To obtain correct description of the far field pattern, one could calculate the induced current density and subsequently the vector potential  $\mathbf{A}(\mathbf{r}, t)$ , which is required for the full description of electromagnetic radiation.

As the quasi-static relations between induced density, potential and electric field are linear in time, they may be equivalently Fourier transformed to frequency space. The induced density is conveniently described in frequency space, c.f. (2.15), and the Hartree potential (2.33) can be equivalently solved from Poisson's equation

$$\nabla^2 \delta\phi(\mathbf{r}, \omega) = -4\pi\delta\rho(\mathbf{r}, \omega), \quad (2.34)$$

from which the induced electric field is obtained as

$$\delta\mathbf{E}(\mathbf{r}, \omega) = -\nabla\delta\phi(\mathbf{r}, \omega), \quad (2.35)$$

similarly to the relation in time space. The electric field enhancement factor is defined as a ratio between the total electric field and the perturbing electric field, i.e.

$$\text{FE}(\mathbf{r}, \omega) = \frac{|\mathbf{E}_{\text{ext}}(\mathbf{r}, \omega) + \delta\mathbf{E}(\mathbf{r}, \omega)|}{|\mathbf{E}_{\text{ext}}(\mathbf{r}, \omega)|}, \quad (2.36)$$

where in the dipole approximation the perturbing field is spatially constant, i.e.  $\mathbf{E}_{\text{ext}}(\mathbf{r}, \omega) = \mathbf{E}_{\text{ext}}(\omega)$ , c.f. (2.6).

Although the induced electric field is particularly strong when the external field is tuned to the plasmon resonance frequency, the field enhancement is not necessarily negligible either at smaller frequencies, when the charge density oscillations and the induced electric field are in-phase with the external field. This fact is demonstrated in Section 5.1 for molecular metal chains.



### 3 Time-dependent density functional theory

Time-dependent density functional theory (TDDFT) is a reformulation of the many-body quantum mechanics described by the time-dependent Schrödinger equation (2.1) and the Hamiltonian (2.2) in terms of time-dependent electron density  $n_\sigma(\mathbf{r}, t)$ . TDDFT can be considered as an extension of density functional theory (DFT), which accounts only for the time-independent Schrödinger equation (2.4) providing a basis for time-dependent calculations.

In Sections 3.1 and 3.2 the formal justification and practical Kohn-Sham description of the density functional theory and its time-dependent extension are presented. Practical time and frequency domain schemes of TDDFT for the study of electronic excitations are introduced in Sections 3.3 and 3.4.

The formalism is presented for the spin-polarized case, but since the external potentials considered in this work are spin-independent, c.f. (2.3) and (2.6), the formulation in terms of total electron density  $n(\mathbf{r}, t) = \sum_\sigma n_\sigma(\mathbf{r}, t)$  would be equally valid. The inclusion of spin-dependence leads to slightly cumbersome notation here and there, but it is worthwhile as the computational implementations of the present work support spin-polarized calculations, see Section 4.2.

#### 3.1 Ground state: Density functional theory

Density functional theory (DFT) is a many-body quantum mechanical theory, where the fundamental quantity is electron density  $n_\sigma(\mathbf{r})$ , instead of the many-body wave function  $\Psi_{\sigma_1 \dots \sigma_N}(\mathbf{r}_1, \dots, \mathbf{r}_N)$  introduced in the Schrödinger equation (2.4). In the theory level, DFT is valid for any system of identical particles with any interaction, but only electronic system described by the Hamiltonian  $\hat{\mathcal{H}}_0$ , c.f. (2.5), is considered. [45, ch. 6]

The foundation of DFT lies in theorems first proved by Hohenberg and Kohn [80] for spin-paired systems and later generalized to the spin-polarized case [81]. The theorems state that the ground state particle density of the system,  $n_\sigma^0(\mathbf{r})$  (both spin components), uniquely determines the external potential  $v_\sigma^{\text{ext}}(\mathbf{r})$ . Thus  $n^0$  also determines the whole Hamiltonian (2.5) and the many-body wave function  $\Psi$ , which is given uniquely by the Schrödinger equation. According to the axioms of quantum mechanics,  $\Psi$ , and hence  $n^0$ , contains all information on the system. Additionally, there exists a functional of density  $E[n_\uparrow, n_\downarrow]$ , valid for any external potential  $v_\sigma^{\text{ext}}(\mathbf{r})$ , whose global minimum value is the exact ground state energy  $E_0$  and the corresponding density is the exact ground state density  $n_\sigma^0(\mathbf{r})$ . Thus, the functional  $E[n_\uparrow, n_\downarrow]$  is enough to determine all properties of the system. [45, ch. 6]

However, the proofs of the Hohenberg-Kohn theorems provide no construction of the functional  $E[n_\uparrow, n_\downarrow]$ . The practical approach of DFT theory bases on an auxiliary independent-particle system introduced by Kohn and Sham. [82] By construction, the Kohn-Sham system is supposed to have the same ground state density as the original many-body system. The Kohn-Sham system is described by an independent particle Schrödinger-like equation

$$h^{\text{KS}} \psi_{i\sigma}(\mathbf{r}) = \epsilon_{i\sigma} \psi_{i\sigma}(\mathbf{r}), \quad (3.1)$$

which defines the Kohn-Sham wave functions  $\psi_{i\sigma}$  and eigenenergies  $\epsilon_{i\sigma}$ . The effective Kohn-Sham Hamiltonian is

$$h^{\text{KS}} = \underbrace{-\frac{1}{2}\nabla^2}_{t^{\text{KS}}} + \underbrace{\int d\mathbf{r}' \frac{\sum_{\tau} n_{\tau}(\mathbf{r}')}{|\mathbf{r} - \mathbf{r}'|}}_{v^{\text{H}}[n](\mathbf{r})} + \underbrace{v_{\sigma}^{\text{ext}}(\mathbf{r}) + v_{\sigma}^{\text{xc}}[n_{\uparrow}, n_{\downarrow}](\mathbf{r})}_{v_{\sigma}^{\text{KS}}[n_{\uparrow}, n_{\downarrow}](\mathbf{r})}, \quad (3.2)$$

which contains explicitly the independent-particle kinetic energy  $t^{\text{KS}}$  and the long-range Hartree potential  $v^{\text{H}}$  corresponding to classical Coulomb interaction energy. Single-particle external potential is the same as in the original system, i.e.  $v_{\sigma}^{\text{ext}}(\mathbf{r})$  in (2.3) and (2.5). The exchange-correlation potential  $v_{\sigma}^{\text{xc}}[n_{\uparrow}, n_{\downarrow}]$  is defined to contain all missing many-body aspects of the original system. By the Hohenberg-Kohn theorems applied to the non-interacting Kohn-Sham system, the exchange-correlation potential  $v_{\sigma}^{\text{xc}}$  is in principle a functional of the spin-dependent density  $n_{\sigma}(\mathbf{r})$  alone. [45, ch. 7]

By definition, it is clear that it is not straightforward to write down an exact form for the exchange-correlation potential  $v_{\sigma}^{\text{xc}}[n_{\uparrow}, n_{\downarrow}]$ . However, if it were known, or a suitable approximation to it is at hand, then the independent particle Kohn-Sham wave functions  $\psi_{i\sigma}$  can be solved from (3.1). The ground state is obtained by assigning the  $N = N_{\uparrow} + N_{\downarrow}$  electrons to the  $N_{\sigma}$  lowest orbitals  $\psi_{i\sigma}$  in energy  $\epsilon_{i\sigma}$  for both spins  $\sigma \in \{\uparrow, \downarrow\}$ , yielding the occupation numbers  $f_{i\sigma}$ . When the external potential  $v_{\sigma}^{\text{ext}}(\mathbf{r})$  is independent of spin  $\sigma$ , as is the case in this work, one may consider the spin channels to be paired in spin-degenerate systems. Then calculations include only one spin channel, say  $\sigma = \uparrow$ , and occupation numbers  $f_{i\sigma}$  are typically 2. However, the spin-paired approach is not valid for e.g. magnetic systems where the spin-degeneracy is lifted. [45, ch. 7]

The Kohn-Sham Hamiltonian (3.2) depends on solutions  $\psi_{i\sigma}$  through the density

$$n_{\sigma}(\mathbf{r}) = \sum_i f_{i\sigma} |\psi_{i\sigma}(\mathbf{r})|^2, \quad (3.3)$$

whence the equations (3.1) and (3.2) has to be iterated to obtain a self-consistent solution. Once the self-consistency is achieved, the ground state electron density is given by (3.3). [45, ch. 7]

The success of DFT is thanks to the success of the approximations to the exchange-correlation potential  $v^{\text{xc}}$ . In the Kohn-Sham Hamiltonian (3.2) the independent particle kinetic energy  $t^{\text{KS}}$  and the long range Hartree potential  $v^{\text{H}}$  have been explicitly included from the underlying many-body problem. As a consequence it has been found out that even relatively simple approximations for  $v^{\text{xc}}$  yield surprisingly good results. The initial workhorse has been the local spin density approximation (L(S)DA) and its spin-paired counterpart local density approximation (LDA) which is derived from the properties of the homogeneous electron gas. Generalized-gradient approximation (GGA) is a family of functionals that are generalizations of LDA, adding functional dependence also on the gradient of the density. The PBE functional [83] used in this work is a GGA functional. Also non-local functionals

have been designed, as well as so called orbital-dependent functionals that depend not only on the density but also on the Kohn-Sham wave functions  $\psi_{i\sigma}$  similarly to the Kohn-Sham kinetic energy  $t^{\text{KS}}$ , although  $v^{\text{xc}}$  is in principle a functional of the density alone. [45, ch. 8]

### 3.2 Extending to time dependent case

Time-dependent density functional theory (TDDFT) is a time-dependent extension of DFT. Analogously to the Hohenberg-Kohn theorem in the time-independent case, there exist a theorem by Runge and Gross [84] stating that for a given initial state  $\Psi_0$  the time-dependent density  $n_\sigma(\mathbf{r}, t)$  uniquely determines the external potential  $v_\sigma^{\text{ext}}(\mathbf{r}, t)$  and hence all properties of the evolving system. The theorem is applicable to any system of identical particles with any temporally fixed interaction, but for simplicity only electronic systems are considered in this work. [44, ch. 4] In addition, to be strict, the original Runge-Gross theorem considers only spin-paired case but it has been generalized to spin-polarized case also [85].

Similarly to the Kohn-Sham approach to DFT, an independent-particle Kohn-Sham system is introduced in TDDFT, with the assumption that it reproduces exactly the time-dependent density of the many-body system. The time-dependent Kohn-Sham equations are

$$h^{\text{KS}} \psi_{i\sigma}(\mathbf{r}, t) = i \frac{\partial}{\partial t} \psi_{i\sigma}(\mathbf{r}, t), \quad (3.4)$$

and

$$h^{\text{KS}} = -\frac{1}{2} \nabla^2 + \underbrace{\int d\mathbf{r}' \frac{\sum_\tau n_\tau(\mathbf{r}', t)}{|\mathbf{r} - \mathbf{r}'|} + v_\sigma^{\text{ext}}(\mathbf{r}, t) + v_\sigma^{\text{xc}}[n_\uparrow, n_\downarrow; \Psi_0, \Phi_0](\mathbf{r}, t)}_{v_\sigma^{\text{KS}}(\mathbf{r}, t)} \quad (3.5)$$

analogously to (3.1) and (3.2). The density is given as  $n_\sigma(\mathbf{r}, t) = \sum_i f_{i\sigma} |\psi_{i\sigma}(\mathbf{r}, t)|^2$ , like in (3.3). The exchange-correlation potential  $v_\sigma^{\text{xc}}[n_\uparrow, n_\downarrow; \Psi_0, \Phi_0]$  depends on the initial states of the many-body system  $\Psi_0$  and that of the Kohn-Sham system  $\Phi_0$ , which can be chosen to be e.g. Slater determinant of the single-particle Kohn-Sham wave functions. However, usually the initial state is chosen to be the ground state of the system, when both  $\Psi_0$  and  $\Phi_0$  are uniquely determined by the ground state density as stated by the Hohenberg-Kohn theorem. Then, the exchange-correlation potential is a functional of density alone. [44, ch. 4]

Additional complication is that the exchange-correlation potential  $v_\sigma^{\text{xc}}$  is a functional of the whole history of the time-dependent density. This memory effect is neglected in the adiabatic functionals, which are obtained from the ground state exchange-correlation functional by using instantaneous density in ground state functionals. For example, adiabatic LDA functional is given by

$$v^{\text{xc,ALDA}}[n](\mathbf{r}, t) = v^{\text{xc,LDA}}[n(t)](\mathbf{r}). \quad (3.6)$$

Other adiabatic functionals, e.g. adiabatic GGA, are obtained similarly from the ground state equivalents. Adiabatic functionals perform surprisingly well in many

cases, in spite of their simplicity. [44, ch. 4] However, functionals with history dependence have also been devised to describe e.g. double-excitations that are not captured by adiabatic functionals. [44, ch. 8]

After an appropriate approximation for the exchange-correlation potential  $v_{\sigma}^{\text{xc}}$  has been chosen, the time-dependent Kohn-Sham equations (3.4) and (3.5) can be solved for a given initial condition to obtain the time evolution of the Kohn-Sham density from which, according to the Runge-Gross theorem, any dynamic property of the system can be obtained, at least in principle. This kind of TDDFT approaches have been used to study response properties even before the formal justification was given by Runge and Gross in 1984 [84], see e.g. [86].

In the case of interaction between light and nanostructures, there are two widely used practical approaches for obtaining the response quantities introduced in Section 2 within TDDFT framework. A scheme based on direct propagation of the Kohn-Sham system is described in Section 3.3, whereas in Section 3.4 a solution for the problem directly in the frequency space is described.

### 3.3 Time propagation method

The time propagation method is a direct way to solve the time evolution of the system from the time-dependent Kohn-Sham equations (3.4) and (3.5). After the differential equation (3.4) has been discretized in time, it can be used to propagate the initial Kohn-Sham orbitals with the desired time resolution. [44, ch. 7] Numerically, the choice of the propagation method plays a major role in ensuring the stability of the time propagation [87].

In the time propagation method, the ground state is obtained from standard DFT calculation. Then a perturbation is added to the Hamiltonian and the Kohn-Sham system is propagated in time to obtain  $n_{\sigma}(\mathbf{r}, t)$ , from which the desired properties can be calculated. It should be emphasized that this time propagation method is not limited to linear response regime. Instead, the method always gives the full non-linear response of the system. However, if the perturbation is weak enough, then the linear response is dominant. [44, ch. 7]

The response of the system to the electric field, i.e. the response properties derivable from the density-density response function, c.f. Section 2, can be conveniently obtained from a TDDFT simulation where the time-dependent density  $n_{\sigma}(\mathbf{r}, t)$  is the fundamental quantity. In the time propagation method, it is advantageous to choose the electric field to be a  $\delta$ -pulse perturbation as proposed by Yabana *et al.* [88]. Then  $\mathbf{E}(t) = \mathbf{E}\delta(t)$ , where electric field strength  $|\mathbf{E}|$  is small enough to stay in the linear response regime. The dipolar perturbation is then given by, c.f. (2.6),

$$\delta v^{\text{ext}}(\mathbf{r}, t) = \mathbf{r} \cdot \mathbf{E}\delta(t), \quad (3.7)$$

which is in frequency space

$$\delta v^{\text{ext}}(\mathbf{r}, \omega) = \mathbf{r} \cdot \mathbf{E}, \quad (3.8)$$

i.e., the whole frequency space is covered with a single perturbation. [44, ch. 7]

Using a  $z$  polarized electric field, i.e.  $\delta v^{\text{ext}}(\mathbf{r}, \omega) = zE_z$ , the corresponding induced density, c.f. (2.15), is obtained in Fourier space as

$$\delta n_\sigma^z(\mathbf{r}, \omega) = \int_0^\infty dt \left( n_\sigma^z(\mathbf{r}, t) - n_\sigma^0(\mathbf{r}) \right) e^{i\omega t}, \quad (3.9)$$

where  $n_\sigma^z(\mathbf{r}, t) = n_\sigma^0(\mathbf{r})$ , for  $t < 0$ , and at later times it is given by the time propagation. The polarizability is obtained as, c.f. (2.19),

$$\begin{aligned} \alpha_{xz}(\omega) &= - \sum_\sigma \frac{1}{E_z} \int d\mathbf{r} x \int_0^\infty dt \left( n_\sigma^z(\mathbf{r}, t) - n_\sigma^0(\mathbf{r}) \right) e^{i\omega t} \\ &= \frac{1}{E_z} \int_0^\infty dt \delta\mu_{xz}(t) e^{i\omega t}, \end{aligned} \quad (3.10)$$

where  $\delta\mu_{xz}(t)$  is the induced dipole moment.

In practice, the time propagation cannot be continued indefinitely, so it is stopped after finite time  $T$ . Then it is convenient to introduce damping in the Fourier transform to obtain response in whole frequency space without artificial oscillations due to oversampling in frequency. Thus, in a practical implementation,

$$\alpha_{xz}(\omega) = \frac{1}{E_z} \int_0^T dt \delta\mu_{xz}(t) e^{i\omega t} g(t), \quad (3.11)$$

where  $g(t)$  is a damping function. In essence, the damping function introduces lifetime for the excitations. Thus, no damping would be required if dissipation of energy would be included in the description of the system. Common choices for the damping function are  $g(t) = e^{-\eta t}$  or  $g(t) = e^{-\frac{1}{2}\sigma^2 t^2}$ , leading to Lorentzian or Gaussian line broadening, respectively. [44, ch. 7]

Equation (3.11) is directly feasible in a numerical implementation. One only needs to record the induced dipole moment during the time propagation and then as a post-processing step Fourier transform it to get the polarizability. After the time propagation has been repeated for  $\delta$ -perturbations polarized along all spatial axes,  $x$ ,  $y$  and  $z$ , all components of the polarizability tensor  $\boldsymbol{\alpha}$  are obtained. However, the induced density cannot be calculated similarly from (3.9) since numerical presentation of the density  $n_\sigma(\mathbf{r}, t)$  at each time step requires far more memory than the dipole moment  $\boldsymbol{\mu}(t)$ , which is a single number. Nevertheless, the induced density is an essential quantity for characterizing plasmon resonances and calculating the associated electric field enhancement, c.f. Section 2.5. In this work, a scheme for calculating the induced density was implemented. The implementation is described in detail in Section 4.2.1.

### 3.4 Frequency space methods

The idea in the frequency space methods is to evaluate the response of the Kohn-Sham system directly in frequency space and then relate it to the response of the true many-body system. Since the true density  $\delta n_\sigma(\mathbf{r}, \omega)$  is reproduced correctly

by the Kohn-Sham system, the density-density response functions of the true and Kohn-Sham system,  $\chi$  and  $\chi^{\text{KS}}$ , can be connected by using (2.15), i.e.

$$\sum_{\tau} \int d\mathbf{r}' \chi_{\sigma,\tau}(\mathbf{r}, \mathbf{r}', \omega) \delta v_{\tau}^{\text{ext}}(\mathbf{r}', \omega) = \delta n_{\sigma}(\mathbf{r}, \omega) = \sum_{\tau} \int d\mathbf{r}' \chi_{\sigma,\tau}^{\text{KS}}(\mathbf{r}, \mathbf{r}', \omega) \delta v_{\tau}^{\text{KS}}(\mathbf{r}', \omega). \quad (3.12)$$

Similarly, also higher order response functions of the true system could be connected to those of the Kohn-Sham system. The first-order variation in the Kohn-Sham potential  $v_{\sigma}^{\text{KS}}(\mathbf{r}, t)$ , c.f. (3.5), is in frequency space

$$\delta v_{\sigma}^{\text{KS}}(\mathbf{r}, \omega) = \delta v_{\sigma}^{\text{ext}}(\mathbf{r}, \omega) + \sum_{\tau} \int d\mathbf{r}' \underbrace{\left( \frac{1}{|\mathbf{r} - \mathbf{r}'|} + f_{\sigma,\tau}^{\text{xc}}[n_{\uparrow}^0, n_{\downarrow}^0](\mathbf{r}, \mathbf{r}', \omega) \right)}_{K_{\sigma,\tau}(\mathbf{r}, \mathbf{r}', \omega)} \delta n_{\tau}(\mathbf{r}', \omega). \quad (3.13)$$

Here the exchange and correlation effects introduced by  $v^{\text{xc}}$  are included in the exchange-correlation kernel

$$f_{\sigma,\tau}^{\text{xc}}[n_{\uparrow}^0, n_{\downarrow}^0](\mathbf{r}, \mathbf{r}', \omega) = \int_{-\infty}^{\infty} d(t - t') \underbrace{\frac{\delta v_{\sigma}^{\text{xc}}[n_{\uparrow}, n_{\downarrow}](\mathbf{r}, t)}{\delta n_{\tau}(\mathbf{r}', t')}}_{f^{\text{xc}}(t - t')} \bigg|_{n_{\uparrow/\downarrow} = n_{\uparrow/\downarrow}^0} e^{i\omega(t - t')}, \quad (3.14)$$

where the kernel  $f^{\text{xc}}(t - t')$  is evaluated at the ground state density. Here  $f^{\text{xc}}(t - t')$  depends only on time difference  $(t - t')$  due to time-translation invariance of the ground state, and consequently  $f^{\text{xc}}(\omega)$  depends only on a single frequency variable. In the case of adiabatic approximation, c.f. (3.6), the kernel becomes local in time, i.e.  $f^{\text{xc}}(t - t') \propto \delta(t - t')$  whence  $f^{\text{xc}}$  becomes frequency-independent. [44, ch. 4]

By substituting (3.13) into right hand side of (3.12), one obtains the following equation for the induced density  $\delta n_{\sigma}(\mathbf{r}, \omega)$ :

$$\delta n_{\sigma}(\mathbf{r}, \omega) = \sum_{\tau} \int d\mathbf{r}' \chi_{\sigma,\tau}^{\text{KS}}(\mathbf{r}, \mathbf{r}', \omega) \left( \delta v_{\tau}^{\text{ext}}(\mathbf{r}', \omega) + \sum_{\nu} \int d\mathbf{r}'' K_{\tau,\nu}(\mathbf{r}', \mathbf{r}'', \omega) \delta n_{\nu}(\mathbf{r}'', \omega) \right). \quad (3.15)$$

By expressing the induced densities in (3.15) with the true response functions, i.e. with the left hand side of (3.12), one obtains the following Dyson-like equation for the response function after removing the common term  $\sum_{\tau} \int d\mathbf{r}' \dots \delta v_{\tau}^{\text{ext}}(\mathbf{r}', \omega)$ :

$$\chi_{\sigma,\tau}(\mathbf{r}, \mathbf{r}', \omega) = \chi_{\sigma,\tau}^{\text{KS}}(\mathbf{r}, \mathbf{r}', \omega) + \sum_{\lambda,\nu} \int d\mathbf{r}'' \int d\mathbf{r}''' \chi_{\sigma,\lambda}^{\text{KS}}(\mathbf{r}, \mathbf{r}'', \omega) K_{\lambda,\nu}(\mathbf{r}'', \mathbf{r}''', \omega) \chi_{\nu,\tau}(\mathbf{r}''', \mathbf{r}', \omega). \quad (3.16)$$

The Lehmann representation of response function (2.18) can be easily evaluated for a non-interacting system, so it can be used to calculate the Kohn-Sham response function  $\chi^{\text{KS}}$ . Then, in principle, the true response function  $\chi$  is obtained from (3.16) after a suitable approximation for the exchange-correlation is chosen. [44, ch. 4]

The formalism leading to the Dyson equation (3.16) has been presented with the optical response of nanostructures in mind. However, it should be noted that the

equation is also valid for extended systems. In finite systems, the description of the response function in real spatial space is suitable. However, in extended systems, it is convenient to employ the periodic boundary conditions, Fourier transform spatial degrees of freedom in (3.16) to reciprocal space, and utilize Bloch's theorem in solving the density-density response function. [89]

For finite systems, a practical and widely used frequency space method is Casida method, [51, 90] which uses (3.15) as a starting point. By using the unperturbed Kohn-Sham states  $\psi_{i\sigma}$  as a single-particle basis in second quantization, the induced density can be written in terms of the density matrix as

$$\delta n_{\sigma}(\mathbf{r}, \omega) = \sum_{ij} \psi_{i\sigma}(\mathbf{r}) \psi_{j\sigma}^*(\mathbf{r}) \delta P_{ij\sigma}(\omega). \quad (3.17)$$

Since the basis functions  $\{\psi_{i\sigma}\}$  are fixed, the matrix  $\delta P_{ij\sigma}(\omega)$  uniquely determines the induced density. Analogously, (3.15) can be written in this notation as

$$\delta P_{ij\sigma}(\omega) = -\frac{f_{i\sigma} - f_{j\sigma}}{\omega - (\epsilon_{i\sigma} - \epsilon_{j\sigma})} \left( \delta v_{ij\sigma}^{\text{ext}}(\omega) + \sum_{kl\tau} K_{ij\sigma,kl\tau}(\omega) \delta P_{kl\tau}(\omega) \right), \quad (3.18)$$

where the Kohn-Sham response function  $\chi^{\text{KS}}$  has been evaluated with the Lehmann representation (2.18) in the limit  $\eta \rightarrow 0^+$ . [51] The matrix elements of the perturbing potential and the coupling matrix  $K$  are given by

$$\delta v_{ij\sigma}^{\text{ext}}(\omega) = \int d\mathbf{r} \psi_{i\sigma}^*(\mathbf{r}) \delta v_{\sigma}^{\text{ext}}(\mathbf{r}, \omega) \psi_{j\sigma}(\mathbf{r}) \quad (3.19)$$

and

$$K_{ij\sigma,kl\tau}(\omega) = \int d\mathbf{r} \int d\mathbf{r}' \psi_{i\sigma}^*(\mathbf{r}) \psi_{j\sigma}(\mathbf{r}) K_{\sigma,\tau}(\mathbf{r}, \mathbf{r}', \omega) \psi_{k\tau}(\mathbf{r}') \psi_{l\tau}^*(\mathbf{r}'), \quad (3.20)$$

respectively. For electric field polarized in  $z$  direction, the dipolar perturbation is  $\delta v^{\text{ext}}(\mathbf{r}, \omega) = z E_z(\omega)$ , and (3.19) reads

$$\delta v_{ij\sigma}^{\text{ext}}(\omega) = \int d\mathbf{r} \psi_{i\sigma}^*(\mathbf{r}) z E_z(\omega) \psi_{j\sigma}(\mathbf{r}) = z_{ij\sigma} E_z(\omega) \quad (3.21)$$

The polarizability is obtained with the help of (2.19) and (3.17) as

$$\alpha_{xz}(\omega) = -\frac{1}{E_z(\omega)} \sum_{ij\sigma} x_{ji\sigma} \delta P_{ij\sigma}(\omega), \quad (3.22)$$

where  $x_{ij\sigma} = \int d\mathbf{r} \psi_{i\sigma}^*(\mathbf{r}) x \psi_{j\sigma}(\mathbf{r})$ . [51]

In practical implementation, it is useful to arrange the Kohn-Sham basis  $\{\psi_{i\sigma}\}$  according to the occupation numbers so that  $i < j \Leftrightarrow f_{i\sigma} \geq f_{j\sigma}$ . Then the triple index  $ij\sigma$  with  $i < j$  corresponds to particle-hole (ph) transition  $\psi_{i\sigma} \rightarrow \psi_{j\sigma}$ , since the initial state  $\psi_{i\sigma}$  is more occupied than the final state  $\psi_{j\sigma}$ . The density matrix  $\delta P_{ij\sigma}$  can be correspondingly interpreted as a vector in this particle-hole basis. However,  $\delta P_{ij\sigma}$  contains also the opposite hole-particle transitions. Due to hermiticity of the density matrix, hole-particle transitions can be mapped to particle-hole transitions

by complex conjugation. Thus, by explicitly including only the particle-hole elements in polarizability (3.22) and similar expressions, the computational effort can be cut by half. Then, the polarizability can be rewritten as

$$\alpha_{xz}(\omega) = -\frac{1}{E_z(\omega)} 2 \sum_{ij\sigma}^{f_{i\sigma}-f_{j\sigma}>0} x_{ji\sigma} (\text{Re}[\delta P_{ij\sigma}(t)])(\omega), \quad (3.23)$$

where summation includes only particle-hole elements and  $(\text{Re}[\delta P_{ij\sigma}(t)])(\omega)$  is Fourier transform of the real part of the time space density matrix. The elements with  $f_{i\sigma} - f_{j\sigma} = 0$  lead to  $\delta P_{ij\sigma} = 0$  by (3.18) and thus are not included in the sum. [51]

The  $\delta P_{ij\sigma}(\omega)$  can be solved from (3.18). Casida has shown that the required  $(\text{Re}[\delta P_{ij\sigma}(t)])(\omega)$  is given by

$$(\text{Re}[\delta P_{ij\sigma}(t)])(\omega) = -\sum_I \frac{1}{\omega_I^2 - \omega^2} \sum_{kl\tau}^{\text{ph}} \sqrt{f_{ij\sigma}\omega_{ij\sigma}} F_{I,ij\sigma} F_{I,kl\tau}^* \sqrt{f_{kl\tau}\omega_{kl\tau}} \delta v_{kl\tau}^{\text{ext}}(\omega), \quad (3.24)$$

where shorthands  $f_{ij\sigma} = f_{i\sigma} - f_{j\sigma}$  and  $\omega_{ij\sigma} = \epsilon_{j\sigma} - \epsilon_{i\sigma}$  have been used and "ph" indicates the inequality  $f_{ij\sigma} > 0$ .  $F_I$  and  $\omega_I^2$  are eigenvectors and eigenvalues of a eigenvalue equation

$$\Omega(\omega) F_I = \omega_I^2 F_I, \quad (3.25)$$

where

$$\Omega_{ij\sigma,kl\tau}(\omega) = \omega_{ij\sigma}^2 \delta_{ij\sigma,kl\tau} + 2\sqrt{f_{ij\sigma}\omega_{ij\sigma}} K_{ij\sigma,kl\tau}(\omega) \sqrt{f_{kl\tau}\omega_{kl\tau}}, \quad (3.26)$$

is a matrix in particle-hole basis, i.e. triple index  $ij\sigma$  correspond only to particle-hole Kohn-Sham transitions, i.e.  $f_{ij\sigma} > 0$ . The triple index Kronecker delta is  $\delta_{ij\sigma,kl\tau} = \delta_{i,k} \delta_{j,l} \delta_{\sigma,\tau}$ . [51]

By substituting (3.24) to (3.23) with the perturbation (3.21), one obtains

$$\alpha_{xz}(\omega) = \sum_I \frac{1}{\omega_I^2 - \omega^2} 2 \underbrace{\sum_{ij\sigma,kl\tau}^{\text{ph}} x_{ij\sigma}^* \sqrt{f_{ij\sigma}\omega_{ij\sigma}} F_{I,ij\sigma} F_{I,kl\tau}^* \sqrt{f_{kl\tau}\omega_{kl\tau}} z_{kl\tau}}_{f_{I,xz}}. \quad (3.27)$$

The poles and residues of the polarizability,  $\omega_I$  and  $f_{I,xz}$ , respectively, yield the excitation energies and oscillator strengths of the true many-body system as is emphasized by comparing (3.27) to (2.20). [51]

In similar fashion, one can obtain the induced density from (3.17). However, this will lead to an expression that is divergent at excitation frequencies as is the polarizability in (3.27) due to term  $1/(\omega_I^2 - \omega^2)$ . This problem can be avoided by recovering a finite lifetime  $\eta$  in the divergent term. Such approach is implemented in the present work. The implemented method and practical aspects of the induced density calculation are described in detail in Section 4.2.2.

From practical point of view, the frequency dependence of the  $\Omega(\omega)$  matrix is problematic since the eigenvalue problem (3.25) is not a simple eigenvalue problem but rather a nonlinear one. [44, ch. 7] However, for adiabatic exchange-correlation,



c.f. discussion after (3.14), the coupling matrix  $K_{ij\sigma,kl\tau}$  and hence  $\Omega$  become frequency independent and the eigenvectors and eigenvalues of the  $\Omega$  matrix can be solved with standard numerical techniques.

Additionally, in practical implementation, the number of Kohn-Sham transitions included in the  $\Omega$  matrix has to be truncated. The most demanding task in Casida method is the calculation of the coupling matrix  $K$  including Coulombic and exchange-correlation integrals. When a real space grid of  $N_R$  grid points is used to represent wave functions  $\psi_{i\sigma}$ , the calculation of  $K$  matrix scales as  $\sim N_R(N_i N_a)^2$ , where  $N_i$  and  $N_a$  are the number of occupied and unoccupied Kohn-Sham states, respectively. In contrary, the time propagation method, where unoccupied Kohn-Sham states need not to be propagated, scales as  $\sim N_R N_i$ . However, the time propagation method has much larger scaling prefactor than Casida method. Thus, Casida method is usually faster for smaller systems whereas the time propagation method is faster for larger systems. However, the exact crossover between *small* and *large* depends greatly on the implementation of the methods, the hardware used and the system in consideration. [91, ch. 15]

## 4 Computational methods

Density functional theory has become a popular first principles tool since its invention, and consequently, there are many different implementations of the formalism. In this work, a highly parallelizable GPAW [92–95] is used.

GPAW uses a uniform three dimensional real space grid to present the wave functions. In addition, it has also support for plane wave basis and localized atomic orbital basis. Other possible choices for numerical representation of wave functions would include other spatial meshes or different basis function sets. GPAW employs projector augmented wave (PAW) method to transform the Kohn-Sham wave functions, which exhibit rapid oscillations near atom nuclei, to smooth pseudo wave functions. The PAW formalism is described in Section 4.1. Alternative approach for mapping the numerically inconvenient Kohn-Sham wave functions to smoother alternatives is to use smooth pseudo potentials for atom sites, although this approach has a drawback that the true Kohn-Sham wave functions are lost whereas in PAW formalism they are recoverable. In extreme case, the whole ionic background potential may be replaced with uniform positive charge density, which is called the jellium approximation. [45]

The uniform grid description in GPAW allows it to parallelize well over the simulation domain, as well as to use efficient multigrid solver for solving the Poisson’s equation, which yields the Hartree potential  $v^H(\mathbf{r})$ , c.f. (3.2). GPAW supports calculations for infinite systems by employing periodic boundary conditions and Bloch’s theorem to sample over the first Brillouin zone in the reciprocal space. However, for the finite nanostructures considered in this work, zero boundary conditions are used for the simulation domain.

The user interface in GPAW is based on Python programming language, and most of the codebase is also written in Python. However, the computationally demanding routines are written in more efficient C language. The computational methods implemented in this work, see Section 4.2, are written in Python. However, the computationally demanding tasks, such as solving the Poisson’s equation, applying gradient operator or adding PAW corrections, are actually readily implemented in GPAW as C functions that are called from Python, making the implementation efficient. GPAW utilizes also Atomic Simulation Environment (ASE) [96, 97] to present the simulation domain and atoms’ positions. ASE provides also general routines for e.g. I/O and a plenty of algorithms for e.g. structure optimization.

### 4.1 Projector augmented wave method

A direct solution of the Kohn-Sham equations (3.1) and (3.2) involves numerical difficulties. The single-particle Kohn-Sham wave functions  $\psi_{i\sigma}(\mathbf{r})$  have rapid oscillations in the atomic regions near the nuclei of the system. On the other hand, far from the nuclei, in the bonding region between atoms, the wave functions are rather smooth. Consequently, their accurate description on a real space grid would require an extremely fine grid near the nuclei whereas in the bonding region a coarser grid would suffice. Thus, instead of using a fine grid over the whole real space, it is feasible to describe near-nuclei region differently from the bonding region. The pro-

jector augmented wave (PAW) method invented by Blöchl [98] is such approach for describing the Kohn-Sham system. [99]

The PAW method bases on a transformation which replaces the rapidly oscillating wave function part around atom  $a$ ,  $\psi_{n\sigma}^a(\mathbf{r})$ , with its smooth counterpart  $\tilde{\psi}_{n\sigma}^a(\mathbf{r})$ , for each atom in the system. The resulting pseudo wave function  $\tilde{\psi}_{n\sigma}(\mathbf{r})$  is smooth over the whole space and hence numerically convenient. By construction, the true wave function is related to the pseudo wave function through

$$\psi_{n\sigma}(\mathbf{r}) = \tilde{\psi}_{n\sigma}(\mathbf{r}) + \sum_a \left( \psi_{n\sigma}^a(\mathbf{r}) - \tilde{\psi}_{n\sigma}^a(\mathbf{r}) \right), \quad (4.1)$$

where  $a$  enumerates the atoms of the system. As the rapid oscillations are localized around each atom, atom-centered augmentation spheres of radii  $r_c^a$  are defined for each atom  $a$  so that  $\tilde{\psi}_{n\sigma}^a(\mathbf{r})$  and  $\psi_{n\sigma}^a(\mathbf{r})$  are equal outside the sphere and  $\tilde{\psi}_{n\sigma}^a(\mathbf{r})$  is smoothly continued inside the sphere. Then  $\sum_a \left( \psi_{n\sigma}^a(\mathbf{r}) - \tilde{\psi}_{n\sigma}^a(\mathbf{r}) \right)$  is an atom-wise local correction to the pseudo wave function. [99]

The basic idea in constructing the atom-wise corrections is to employ the fact that the surrounding chemical environment alters the wave functions significantly only in the bonding region whereas near the atom core the form of the wave functions remain rather unaffected from the inert environment. Consequently,  $\psi_{n\sigma}^a(\mathbf{r})$  can be represented in a partial wave basis  $\phi_i^a(\mathbf{r})$  consisting of the wave functions of the corresponding isolated atom. A smooth continuation of the partial waves to the region inside the augmentation sphere provides the pseudo partial waves  $\tilde{\phi}_i^a(\mathbf{r})$  as a basis for  $\tilde{\psi}_{n\sigma}^a(\mathbf{r})$ . So, the atom-wise correction can be written in partial wave basis as

$$\left( \psi_{n\sigma}^a(\mathbf{r}) - \tilde{\psi}_{n\sigma}^a(\mathbf{r}) \right) = \sum_i \left( \phi_i^a(\mathbf{r}) - \tilde{\phi}_i^a(\mathbf{r}) \right) \langle \tilde{p}_i^a | \tilde{\psi}_{n\sigma} \rangle, \quad (4.2)$$

where  $\langle \tilde{p}_i^a | \tilde{\psi}_{n\sigma} \rangle = \int d\mathbf{r} \tilde{p}_i^{a*}(\mathbf{r}) \tilde{\psi}_{n\sigma}(\mathbf{r})$  are expansion coefficients that are obtained from the pseudo wave function by smooth projector functions  $\tilde{p}_i^a(\mathbf{r})$ . With these choices, (4.1) can be written as

$$|\psi_{n\sigma}\rangle = \mathcal{T} |\tilde{\psi}_{n\sigma}\rangle, \quad \mathcal{T} = 1 + \sum_a \sum_i \left( |\phi_i^a\rangle - |\tilde{\phi}_i^a\rangle \right) \langle \tilde{p}_i^a|, \quad (4.3)$$

which defines the transformation operator  $\mathcal{T}$ . In practice, the summation over  $i$  needs to be truncated, i.e. finite partial wave basis  $\phi_i^a(\mathbf{r})$  is used for each atom. Hence, the used partial waves do not provide complete basis for the wave function, and the transformation between the pseudo and the true wave functions is not strictly exact. However in practice, a small number of partial waves  $\phi_i^a(\mathbf{r})$  turns out to be sufficient for describing the wave function as they are chosen to be isolated atom wave functions. [99]

So called frozen-core approximation can be employed in connection to the PAW method. In this approximation, only the valence states are explicitly calculated. The core electrons in the inner shells of an atom are assumed to stay in the isolated-atom states as their contribution to the bonding should be negligible. So, the core electrons are assumed to have fixed wave functions  $\phi_{i,c}^a$  with smooth counterparts  $\tilde{\phi}_{i,c}^a$ , which coalesce with  $\phi_{i,c}^a$  outside the augmentation sphere. [99]

By using the transformation  $\mathcal{T}$ , the Kohn-Sham Schrödinger equation (3.1) can be rewritten in terms of the pseudo wave functions  $\tilde{\psi}_{n\sigma}$  as

$$\mathcal{T}^\dagger h^{\text{KS}} \mathcal{T} |\tilde{\psi}_{n\sigma}\rangle = \epsilon_{n\sigma} \mathcal{T}^\dagger \mathcal{T} |\tilde{\psi}_{n\sigma}\rangle. \quad (4.4)$$

Thus, by replacing the original Hamiltonian  $h^{\text{KS}}$  with the transformed one  $\mathcal{T}^\dagger h^{\text{KS}} \mathcal{T}$ , the Schrödinger equation can be solved so that only the numerically convenient pseudo wave functions are involved. However, additional complication arises from the fact that (4.4) is no more ordinary eigenvalue equation due to the overlap operator  $\mathcal{T}^\dagger \mathcal{T}$  on the right hand side. Nevertheless, after the self-consistent solution is obtained, the true wave functions can be recovered from the pseudo wave functions by adding the atom-wise local corrections according to (4.1). [99]

Instead of using the true wave functions for calculating desired properties of the system, it is useful to write out expressions for the expectation values of observables in terms of pseudo wave functions and the local corrections, in analogy to the wave function in (4.1). For example, the electron density, which is of special interest in density functional theory and in this work, can be expressed as

$$n_\sigma(\mathbf{r}) = \tilde{n}_\sigma(\mathbf{r}) + \sum_a (n_\sigma^a(\mathbf{r}) - \tilde{n}_\sigma^a(\mathbf{r})). \quad (4.5)$$

Here the pseudo density is

$$\tilde{n}_\sigma(\mathbf{r}) = \sum_n f_{n\sigma} |\tilde{\psi}_{n\sigma}(\mathbf{r})|^2 + \sum_a \tilde{n}_{\sigma,c}^a(\mathbf{r}), \quad (4.6)$$

where  $\tilde{n}_{\sigma,c}^a(\mathbf{r}) = \frac{1}{2} \sum_i |\tilde{\phi}_{i,c}^a(\mathbf{r})|^2$  is smooth core density. The atom-wise local correction in (4.5) is

$$(n_\sigma^a(\mathbf{r}) - \tilde{n}_\sigma^a(\mathbf{r})) = \sum_{ij} D_{\sigma ij}^a \left( \phi_j^{a*}(\mathbf{r}) \phi_i^a(\mathbf{r}) - \tilde{\phi}_j^{a*}(\mathbf{r}) \tilde{\phi}_i^a(\mathbf{r}) \right) + \left( n_{\sigma,c}^a(\mathbf{r}) - \tilde{n}_{\sigma,c}^a(\mathbf{r}) \right), \quad (4.7)$$

where  $n_{\sigma,c}^a(\mathbf{r}) = \frac{1}{2} \sum_i |\phi_{i,c}^a(\mathbf{r})|^2$  is the true core density analogously to its smooth counterpart and the matrix  $D_{\sigma ij}^a = \sum_n \langle \tilde{p}_i^a | \tilde{\psi}_{n\sigma} \rangle f_{n\sigma} \langle \tilde{\psi}_{n\sigma} | \tilde{p}_j^a \rangle$ . [99]

The total charge density of the system is given by, c.f. (2.8),

$$\rho(\mathbf{r}) = - \sum_\sigma n_\sigma(\mathbf{r}) - \sum_a Z^a(\mathbf{r}), \quad (4.8)$$

where  $Z^a(\mathbf{r}) = -Z^a \delta(\mathbf{r} - \mathbf{R}^a)$  is the negative charge distribution of the nucleus with charge  $Z^a$  and position  $\mathbf{R}^a$ . The charge density is an useful quantity in numerical implementation, since in the Kohn-Sham Hamiltonian (3.2) the Coulombic interaction term  $v^{\text{H}}[n_\sigma](\mathbf{r})$  and the electron-nucleus interactions in the external potential  $v_\sigma^{\text{ext}}(\mathbf{r})$  (c.f. (2.3)), can be combined with (4.8) to

$$v^{\text{H}}[\rho](\mathbf{r}) = - \int d\mathbf{r}' \frac{\sum_\sigma n_\sigma(\mathbf{r}')}{|\mathbf{r} - \mathbf{r}'|} + \sum_a \frac{Z^a}{|\mathbf{r} - \mathbf{R}^a|} = \int d\mathbf{r}' \frac{\rho(\mathbf{r}')}{|\mathbf{r} - \mathbf{r}'|}. \quad (4.9)$$

Instead of directly evaluating the Hartree potential from (4.9), the Hartree potential is numerically calculated more efficiently from Poisson's equation  $\nabla^2 v^{\text{H}}(\mathbf{r}) = -4\pi\rho(\mathbf{r})$  by e.g. multigrid techniques. [99]

In PAW formalism, the nuclear contribution to the pseudo charge density is defined specially. The pseudo charge density is defined by

$$\tilde{\rho}(\mathbf{r}) = -\sum_{\sigma} \tilde{n}_{\sigma}(\mathbf{r}) - \sum_a \tilde{Z}^a(\mathbf{r}), \quad (4.10)$$

where  $\tilde{Z}^a(\mathbf{r})$  is the compensation charge density of nucleus  $a$ . By (4.5), the charge densities given by (4.8) and (4.10) are connected as

$$\rho(\mathbf{r}) = \tilde{\rho}(\mathbf{r}) - \underbrace{\sum_a \left( \left( \sum_{\sigma} n_{\sigma}^a(\mathbf{r}) + Z^a(\mathbf{r}) \right) - \left( \sum_{\sigma} \tilde{n}_{\sigma}^a(\mathbf{r}) + \tilde{Z}^a(\mathbf{r}) \right) \right)}_{\Delta\tilde{\rho}^a(\mathbf{r})}. \quad (4.11)$$

The compensation charges are chosen to be such atom-wise local functions that the correction  $\Delta\tilde{\rho}^a(\mathbf{r})$  has a vanishing multipole expansion outside the augmentation sphere of the atom site  $a$ . As a consequence, the pseudo Hartree potential  $\tilde{v}^H(\mathbf{r})$ , defined by  $\nabla^2 \tilde{v}^H(\mathbf{r}) = -4\pi\tilde{\rho}(\mathbf{r})$ , equals to the true Hartree potential outside the augmentation spheres. In other words, the potential due to correction  $\Delta\tilde{\rho}^a(\mathbf{r})$  is non-zero only inside the augmentation sphere, i.e. this choice of the compensation charge density decouples the local charge corrections of different atom sites from each other, leading to simplification in calculations. [99] The use of compensation charges is also profitable in the methods implemented in the present work as described in the next section.

## 4.2 Implementation of the field enhancement calculation

The photoabsorption spectrum calculation has already been implemented in GPAW both in the time propagation and in the Casida formulations [94, 95], which have been described in Sections 3.3 and 3.4. Consequently, the propagation of the Kohn-Sham equations (3.4) and (3.5) as well as the construction and diagonalization of Casida eigenvalue equation (3.25) have already been implemented in GPAW. In this work, this machinery is employed for the field enhancement calculation.

The key quantity for the field enhancement is the induced charge density  $\delta\rho(\mathbf{r}, \omega)$ , from which the induced electric potential, electric field and field enhancement,  $\delta\phi(\mathbf{r}, \omega)$ ,  $\delta\mathbf{E}(\mathbf{r}, \omega)$  and  $\text{FE}(\mathbf{r}, \omega)$ , respectively, can be calculated as given by (2.34)–(2.36) in Section 2.5. Required computational tools, a solver for the Poisson’s equation and the gradient operator, have already been implemented in GPAW. The induced charge density is not straightforwardly obtained, and in Sections 4.2.1 and 4.2.2, the implemented schemes for calculating the induced density  $\delta\rho(\mathbf{r}, \omega)$  within PAW method are described.

However, one technical detail regarding to the numerical calculation of the induced electric potential  $\delta\phi(\mathbf{r}, \omega)$  should be mentioned. For finite systems, the Poisson solver implemented in GPAW employs zero boundary conditions for the potential. However, for typical sizes of vacuum needed to accurately solve the ground state and time-dependent systems, the simulation domain is so small that the induced potential approaches zero too quickly, which leads to distorted electric near field. To overcome this technical restriction, a following approach is implemented: before

solving the Poisson's equation, the simulation domain is temporarily extended by adding more vacuum around the structure. Then the induced potential and electric field are calculated in this larger simulation domain, and afterwards the calculated quantities may be cut to the original simulation domain size to save memory. Alternative approach for lifting the zero boundary conditions from Poisson solver could be to use e.g. analytical multipole moment expansion for the potential and use this expansion for describe potential outside the simulation domain [100].

#### 4.2.1 Time propagation method

The time propagation method based on  $\delta$ -pulse perturbation [88] has been described in Section 3.3. The dynamical polarizability can be efficiently calculated by recording the dipole moment  $\boldsymbol{\mu}(t)$  in each time step and then invoking (3.11) to get the polarizability at a desired frequency  $\omega$ . In principle, one could analogously record  $\rho(\mathbf{r}, t)$  at each time step and after time propagation calculate the frequency dependent induced density

$$\delta\rho(\mathbf{r}, \omega) = \int_0^T dt \left( \rho(\mathbf{r}, t) - \rho^0(\mathbf{r}) \right) e^{i\omega t} g(t), \quad (4.12)$$

where  $g(t)$  is a damping function, e.g.  $g(t) = e^{-\eta t}$  or  $g(t) = e^{-\frac{1}{2}\sigma^2 t^2}$ , c.f. (3.11). However, the large storage requirement for storing  $\rho(\mathbf{r}, t)$  at all time steps strongly inhibits the practical use of this approach.

Instead, the frequency response of the induced density can be efficiently obtained during the time propagation at a fixed set of frequencies  $\{\omega_l\}$  with a fixed damping function  $g(t)$ . In the time propagation scheme, the continuous time is discretized to time steps,  $\Delta t_i$ . At the  $N$ :th step at time  $t_N = \sum_{i=1}^N \Delta t_{i-1}$  ( $t_0 = 0$ ), the finite-time Fourier transform (4.12) can be evaluated as

$$\delta\rho^N(\mathbf{r}, \omega) = \sum_{i=1}^N \Delta t_{i-1} \left( \rho(\mathbf{r}, t_i) - \rho^0(\mathbf{r}) \right) e^{i\omega t_i} g(t_i), \quad (4.13)$$

which can be rewritten in a recursive form

$$\delta\rho^N(\mathbf{r}, \omega) = \delta\rho^{N-1}(\mathbf{r}, \omega) + \Delta t_{N-1} \left( \rho(\mathbf{r}, t_N) - \rho^0(\mathbf{r}) \right) e^{i\omega t_N} g(t_N), \quad (4.14)$$

which is easily evaluated at each time step for fixed frequency and damping function. The time propagation scheme provides  $\rho(\mathbf{r}, t_i)$  at each time step, so only two memory consuming arrays  $\delta\rho^N(\mathbf{r}, \omega)$  and  $\rho^0(\mathbf{r})$  are required to store, making the calculation scheme also easily restartable. Similar approach has been used in GPAW's DensityFourierTransform module [92]. The integral (4.12) could be evaluated also with more accurate methods than the one-step method (4.13). However, then the recursive form would require the storage of old densities  $\delta\rho^{N-n}(\mathbf{r}, \omega)$ ,  $n = 2, \dots$ , which would increase the memory requirements of the calculation.

Additional complication arises from the fact that the true charge density  $\rho(\mathbf{r}, t)$  is not instantly available as GPAW makes all calculations in terms of smooth pseudo quantities. Instead of applying the atom-wise local corrections at each time step to obtain the true density, it is computationally convenient to keep the smooth pseudo

quantities as far as possible, since they can be accurately represented on a coarse grid. As the nuclei are fixed in calculations, the induced charge density equals to the induced electron density, i.e. from (2.8)

$$\delta\rho(\mathbf{r},\omega) = -\sum_{\sigma}\delta n_{\sigma}(\mathbf{r},\omega), \quad (4.15)$$

which can be expressed in terms of the induced pseudo density and local corrections by (4.5) and (4.7) as

$$\delta\rho(\mathbf{r},\omega) = -\sum_{\sigma}\delta\tilde{n}_{\sigma}(\mathbf{r},\omega) - \sum_a\sum_{ij}\delta D_{\sigma ij}^a(\omega)\left(\phi_j^{a*}(\mathbf{r})\phi_i^a(\mathbf{r}) - \tilde{\phi}_j^{a*}(\mathbf{r})\tilde{\phi}_i^a(\mathbf{r})\right), \quad (4.16)$$

since the true and pseudo core densities as well as partial waves are fixed functions. The only time dependence in the atom-wise corrections is in  $D_{\sigma ij}^a$ , which is calculated from the time-evolving pseudo wave functions at each time step.

However, instead of applying the *all-electron* corrections as done in (4.16), the compensation charge corrections should also suffice for the field enhancement calculation since by definition, the electrostatic potential created by the pseudo charge density (4.10) equals to the true electrostatic potential outside the augmentation spheres. The electric field is obtained from the potential by local gradient operator, whence the electric field yielded by the pseudo charge density equals the true one outside the augmentation spheres. In GPAW, the compensation charges are given by

$$\tilde{Z}^a(\mathbf{r}) = \sum_L Q_L^a \tilde{g}_L^a(\mathbf{r}), \quad (4.17)$$

where  $\tilde{g}_L^a(\mathbf{r})$  are fixed angular momentum dependent Gaussian functions [95]. Hence, the induced pseudo charge density is obtained from (4.10) and (4.17) as

$$\delta\tilde{\rho}(\mathbf{r},\omega) = -\sum_{\sigma}\delta\tilde{n}_{\sigma}(\mathbf{r},\omega) - \sum_a\sum_L\delta Q_L^a(\omega)\tilde{g}_L^a(\mathbf{r}). \quad (4.18)$$

The coefficients  $Q_L^a$  are related to  $D_{\sigma ij}^a$  by a time-independent linear relation [93, Eqs. (14)–(16)], so the induced coefficients  $\delta Q_L^a(\omega)$  can be obtained from  $\delta D_{\sigma ij}^a(\omega)$  with the same relation as the Fourier transform is a linear operator.

All in all, instead of calculating the true induced charge density, the recursive formulation (4.14) is used to calculate  $\delta\tilde{n}_{\sigma}(\mathbf{r},\omega)$  and  $\delta D_{\sigma ij}^a(\omega)$  during the time propagation at the predefined frequencies  $\{\omega_l\}$ . After the propagation, the smooth function  $\delta\tilde{n}_{\sigma}(\mathbf{r},\omega)$  can be interpolated to a finer grid. Then either the all-electron or compensation charge corrections given by (4.16) and (4.18) are applied, and the induced electric field is calculated. The advantage of the compensation charge corrections is that they are smoother than the full all-electron corrections, and therefore the compensation charge corrected density is described more accurately on a coarser grid than the all-electron corrected one. In addition, by its definition, the compensation charge corrected density yields the correct electric field outside the augmentation spheres, i.e. in the bonding region, which is usually of the most interest. However, if one is interested on the exact behavior of the induced density near the atom cores, then the all-electron corrections should be used. For these reasons, both correction schemes are implemented in the present work.

The major drawback of the method presented here is that the frequencies and damping for the induced density need to be decided beforehand. So, the excitation frequencies of system or other frequencies of interest need to be determined before the induced density calculation. In practice, this requires that the time propagation scheme is first used to obtain the excitation frequencies of the system and then repeated to obtain the induced densities and field enhancements. However, less accurate propagation might suffice for the first propagation as the more accurate photoabsorption spectra is obtained also from the second propagation.

Alternative computationally feasible approach for the field enhancement calculation could be such that the field enhancement or other spatial quantities of interest are calculated after each time step of the propagation, and the full time-evolution of these quantities is recorded only e.g. along symmetry axis of the system or on specific surfaces, so that the storage requirements remain reasonable. After the propagation, these time-dependent quantities can be Fourier transformed to obtain their frequency presentation, analogously to the induced dipole moment calculation.

#### 4.2.2 Casida method

In Casida method, the induced charge density is obtained directly from the linear response of the electron density (3.17) as

$$\delta\rho(\mathbf{r}, \omega) = - \sum_{\sigma} \sum_{ij} \psi_{i\sigma}(\mathbf{r}) \psi_{j\sigma}^*(\mathbf{r}) \delta P_{ij\sigma}(\omega), \quad (4.19)$$

since the atoms are assumed to remain fixed. By restricting the calculation to particle-hole basis only, i.e. by following the steps from (3.22) to (3.27), the induced density can be rewritten as

$$\delta\rho(\mathbf{r}, \omega) = \sum_I \frac{1}{\omega_I^2 - \omega^2} 2 \sum_{ij\sigma, kl\tau}^{\text{ph}} n_{ij\sigma}^*(\mathbf{r}) \sqrt{f_{ij\sigma} \omega_{ij\sigma}} F_{I,ij\sigma} F_{I,kl\tau}^* \sqrt{f_{kl\tau} \omega_{kl\tau}} z_{kl\tau} E_z(\omega), \quad (4.20)$$

where  $n_{ij\sigma}(\mathbf{r}) = \psi_{i\sigma}^*(\mathbf{r}) \psi_{j\sigma}(\mathbf{r})$  is the *pair density*.

The pair density can be evaluated from the pseudo wave functions by substituting (4.1) into the definition and regrouping terms as

$$\begin{aligned} n_{ij\sigma}(\mathbf{r}) &= \tilde{\psi}_{i\sigma}^*(\mathbf{r}) \tilde{\psi}_{j\sigma}(\mathbf{r}) + \sum_a \left( \psi_{i\sigma}^{a*}(\mathbf{r}) \psi_{j\sigma}^a(\mathbf{r}) - \tilde{\psi}_{i\sigma}^{a*}(\mathbf{r}) \tilde{\psi}_{j\sigma}^a(\mathbf{r}) \right) \\ &\quad + \sum_a \underbrace{\left( \tilde{\psi}_{i\sigma}^*(\mathbf{r}) - \tilde{\psi}_{i\sigma}^{a*}(\mathbf{r}) \right)}_{=0, |\mathbf{r}-\mathbf{R}^a| < r_c^a} \underbrace{\left( \psi_{j\sigma}^a(\mathbf{r}) - \tilde{\psi}_{j\sigma}^a(\mathbf{r}) \right)}_{=0, |\mathbf{r}-\mathbf{R}^a| > r_c^a} \\ &\quad + \sum_a \underbrace{\left( \psi_{i\sigma}^{a*}(\mathbf{r}) - \tilde{\psi}_{i\sigma}^{a*}(\mathbf{r}) \right)}_{=0, |\mathbf{r}-\mathbf{R}^a| > r_c^a} \underbrace{\left( \tilde{\psi}_{j\sigma}(\mathbf{r}) - \tilde{\psi}_{j\sigma}^a(\mathbf{r}) \right)}_{=0, |\mathbf{r}-\mathbf{R}^a| < r_c^a} \\ &\quad + \sum_{a \neq b} \underbrace{\left( \psi_{i\sigma}^{a*}(\mathbf{r}) - \tilde{\psi}_{i\sigma}^{a*}(\mathbf{r}) \right)}_{=0, |\mathbf{r}-\mathbf{R}^a| > r_c^a} \underbrace{\left( \psi_{j\sigma}^b(\mathbf{r}) - \tilde{\psi}_{j\sigma}^b(\mathbf{r}) \right)}_{=0, |\mathbf{r}-\mathbf{R}^b| > r_c^b}. \end{aligned} \quad (4.21)$$



Here the three last lines are zero since the multiplied terms are non-zero only on different regions of space as divided by the augmentation spheres. The last line is zero when the augmentation spheres of different atom sites do not overlap. So, the pair density can be partitioned similarly to the electron density, c.f. (4.5),

$$n_{ij\sigma}(\mathbf{r}) = \tilde{n}_{ij\sigma}(\mathbf{r}) + \sum_a \left( n_{ij\sigma}^a(\mathbf{r}) - \tilde{n}_{ij\sigma}^a(\mathbf{r}) \right), \quad (4.22)$$

where  $\tilde{n}_{ij\sigma}(\mathbf{r}) = \tilde{\psi}_{i\sigma}^*(\mathbf{r})\tilde{\psi}_{j\sigma}(\mathbf{r})$ , and the atom-wise correction term is given by, c.f. (4.2),

$$\left( n_{ij\sigma}^a(\mathbf{r}) - \tilde{n}_{ij\sigma}^a(\mathbf{r}) \right) = \sum_{kl} D_{ij\sigma kl}^a \left( \phi_l^{a*}(\mathbf{r})\phi_k^a(\mathbf{r}) - \tilde{\phi}_l^{a*}(\mathbf{r})\tilde{\phi}_k^a(\mathbf{r}) \right), \quad (4.23)$$

where  $D_{ij\sigma kl}^a = \langle \tilde{p}_k^a | \tilde{\psi}_{j\sigma} \rangle \langle \tilde{\psi}_{i\sigma} | \tilde{p}_l^a \rangle$ .

In addition to the full all-electron corrections, also the compensation charges can be defined for the pair density. The compensation charge corrected pair density is given by

$$\tilde{\rho}_{ij\sigma}(\mathbf{r}) = \tilde{n}_{ij\sigma}(\mathbf{r}) + \sum_a \tilde{Z}_{ij\sigma}^a(\mathbf{r}), \quad (4.24)$$

where the compensation charges are similarly to (4.17)

$$\tilde{Z}_{ij\sigma}^a(\mathbf{r}) = \sum_L Q_{ij\sigma L}^a \tilde{g}_L^a(\mathbf{r}). \quad (4.25)$$

The coefficients  $Q_{ij\sigma L}^a$  are obtained from  $D_{ij\sigma kl}^a$  so that in the relation

$$n_{ij\sigma}(\mathbf{r}) = \tilde{\rho}_{ij\sigma}(\mathbf{r}) + \underbrace{\sum_a \left( n_{ij\sigma}^a(\mathbf{r}) - \tilde{n}_{ij\sigma}^a(\mathbf{r}) - \tilde{Z}_{ij\sigma}^a(\mathbf{r}) \right)}_{\Delta\tilde{\rho}_{ij\sigma}^a(\mathbf{r})} \quad (4.26)$$

the correction term  $\Delta\tilde{\rho}_{ij\sigma}^a(\mathbf{r})$  has a vanishing multipole expansion outside the augmentation sphere. [94] Thus, the benefits of the compensation charge corrected pseudo density in comparison to the all-electron corrected one are similar as in the time propagation case, c.f. discussion in Section 4.2.1. For example, the dipole term  $z_{kl\tau}$  in (4.20) can be calculated exactly from the compensation charge corrected density:

$$z_{kl\tau} = \int d\mathbf{r} z n_{kl\tau}(\mathbf{r}) = \int d\mathbf{r} z \tilde{\rho}_{kl\tau}(\mathbf{r}) + \underbrace{\sum_a \int d\mathbf{r} z \Delta\tilde{\rho}_{kl\tau}^a(\mathbf{r})}_{=0}, \quad (4.27)$$

where the atom-wise integrals are zero by the definition of the compensation charges. In addition, the compensation charge part of the matrix element (4.27) can also be calculated analytically as  $\tilde{g}_L^a(\mathbf{r})$  are fixed Gaussian functions. GPAW already includes the calculation of  $z_{kl\tau}$  in this semi-analytical form [94, Eqs. (26)–(27)].

With either the all-electron corrections (4.22) or the compensation charge corrections (4.24), the induced charge density (4.20) can be evaluated. As a practical

detail, a major increase in performance and decrease in memory requirements may be achieved by reordering the summations in (4.20) to

$$\delta\rho(\mathbf{r}, \omega) = \sum_{ij\sigma}^{\text{ph}} n_{ij\sigma}^*(\mathbf{r}) \cdot 2\sqrt{f_{ij\sigma}\omega_{ij\sigma}} \sum_I \frac{1}{\omega_I^2 - \omega^2} F_{I,ij\sigma} \sum_{kl\tau}^{\text{ph}} F_{I,kl\tau}^* \sqrt{f_{kl\tau}\omega_{kl\tau}} z_{kl\tau} E_z(\omega), \quad (4.28)$$

and by implementing this equation from right to left, so that numerical operations on  $n_{ij\sigma}^*(\mathbf{r})$  are minimized. This is desirable as for all triple indices  $ij\sigma$  the numerical grid presentation of the pair density  $n_{ij\sigma}^*(\mathbf{r})$  is a large array.

The induced density (4.20) as well as polarizability (3.27) are divergent at the excitation frequencies  $\omega_I$ . This is due to the infinite lifetime limit  $1/\eta \rightarrow \infty$  that is built in the Casida formulation. However, physically excitations have finite lifetime due to the intrinsic decay of the excited state, leading to Lorentzian line shape in the excitation spectrum. Yet, experimentally observed line shapes have usually Gaussian profile due to imperfection of instruments. However, in some cases the lifetime broadening may be larger than the instrumental broadening and Lorentzian line shapes are observed also experimentally.

To recover the finite lifetime in Casida formulation, following approach is used. The divergent term  $1/(\omega_I^2 - \omega^2)$  originates from the  $\eta \rightarrow 0^+$  limit in the Lehmann representation of the density-density response function (2.18), i.e.

$$\frac{1}{\omega - \omega_I + i\eta} - \frac{1}{\omega + \omega_I + i\eta} \xrightarrow{\eta \rightarrow 0^+} -\frac{2\omega_I}{\omega_I^2 - \omega^2}. \quad (4.29)$$

Thus, the finite lifetime can be recovered to the divergent term through opposite transformation

$$\begin{aligned} \frac{1}{\omega_I^2 - \omega^2} &\xrightarrow{\eta > 0} -\frac{1}{2\omega_I} \left( \frac{1}{\omega - \omega_I + i\eta} - \frac{1}{\omega + \omega_I + i\eta} \right) \\ &= -\frac{\pi}{2\omega_I} \left( \frac{1}{\pi} \frac{\omega - \omega_I}{(\omega - \omega_I)^2 + \eta^2} - \frac{1}{\pi} \frac{\omega + \omega_I}{(\omega + \omega_I)^2 + \eta^2} \right) \\ &\quad + \frac{i\pi}{2\omega_I} \left( \frac{1}{\pi} \frac{\eta}{(\omega - \omega_I)^2 + \eta^2} - \frac{1}{\pi} \frac{\eta}{(\omega + \omega_I)^2 + \eta^2} \right), \end{aligned} \quad (4.30)$$

where real and imaginary parts have been separated. This form satisfies exact conditions required to physical response: the real and imaginary parts are connected through the Kramers-Kronig relations (2.21) (see e.g. [101, p. 459]) and the real part is symmetric and the imaginary part antisymmetric as required for a quantity that is real in time, i.e.  $\delta\rho(\mathbf{r}, t) \in \mathbb{R}$  so  $\delta\rho(\mathbf{r}, \omega) = \delta\rho^*(\mathbf{r}, -\omega)$  and similarly for  $\alpha_{xz}$ .

However, the above approach may not be strictly valid. To be rigorous, one should not take the  $\eta \rightarrow 0^+$  limit in the Lehmann representation but rather keep finite  $\eta$  all way to the end of the response calculations. Nevertheless, the present approach yields excellent results in comparison to the time propagation approach, where the finite lifetime and spectral broadening are introduced by a damping function in Fourier transform, c.f. (4.12), see Section 5.1 for such comparison. However,

an inevitable limitation of the present approach is that the lifetime remains as an arbitrary parameter in calculations. First principles predictions for the lifetime could be obtained with e.g. GW calculations [102].

The formulation (4.30) yields Lorentzian line shape for the excitation spectrum. Correspondingly, the  $\eta$  parameter is equivalent to that of the Lorentzian damping  $g(t) = e^{-\eta t}$  in the time propagation method. To realize the Gaussian line shape, corresponding to  $g(t) = e^{-\frac{1}{2}\sigma^2 t^2}$  in the time propagation, the normalized Lorentzians

$$g_L(\omega) = \frac{1}{\pi} \frac{\eta}{\omega^2 + \eta^2} \quad (4.31)$$

can be replaced by normalized Gaussians

$$g_G(\omega) = \frac{1}{\sqrt{2\pi}\sigma} e^{-\frac{\omega^2}{2\sigma^2}}. \quad (4.32)$$

Then the divergent term is interpreted as

$$\begin{aligned} \frac{1}{\omega_I^2 - \omega^2} \rightarrow & -\frac{\pi}{2\omega_I} \left( \frac{\sqrt{2}}{\pi\sigma} D\left(\frac{\omega - \omega_I}{\sqrt{2}\sigma}\right) - \frac{\sqrt{2}}{\pi\sigma} D\left(\frac{\omega + \omega_I}{\sqrt{2}\sigma}\right) \right) \\ & + \frac{i\pi}{2\omega_I} \left( \frac{1}{\sqrt{2\pi}\sigma} e^{-\left(\frac{\omega - \omega_I}{\sqrt{2}\sigma}\right)^2} - \frac{1}{\sqrt{2\pi}\sigma} e^{-\left(\frac{\omega + \omega_I}{\sqrt{2}\sigma}\right)^2} \right), \end{aligned} \quad (4.33)$$

where  $D(\omega)$  is Dawson integral

$$D(\omega) = e^{-\omega^2} \int_0^\omega ds e^{s^2} \quad (4.34)$$

obtained by the Kramers-Kronig relations from the Gaussian line shape (see e.g. [101, p. 465] and note that  $D(x) = -i\sqrt{\pi}/2 \exp(-x^2) \operatorname{erf}(ix)$ ).

The imaginary part of the divergent term gives the out-of-phase response of the system and yields the dipole strength function (2.32) from the polarizability (3.27). With the interpretation of the divergent term as given by (4.30) or (4.33), the dipole strength function is

$$S_z(\omega) = \sum_I f_{I,zz} \frac{\omega}{\omega_I} (g(\omega - \omega_I) - g(\omega + \omega_I)), \quad (4.35)$$

where  $g(\omega)$  is normalized Lorentzian or Gaussian, (4.31) or (4.32), respectively. This expression can be simplified by small approximations. For  $\omega > 0$ , the off-resonant term  $g(\omega + \omega_I)$  is negligible in comparison to the resonant term  $g(\omega - \omega_I)$ . Additionally,  $g(\omega - \omega_I)$  is peaked at the excitation frequency  $\omega_I$  whence it is justified to approximate  $\omega/\omega_I \approx 1$  in (4.35). With these approximations, (4.35) is simplified to

$$S_z(\omega) = \sum_I f_{I,zz} g(\omega - \omega_I), \quad (4.36)$$

which is the form implemented in the photoabsorption spectrum calculation in GPAW [94]. However, these approximations are not suitable for the real part of the divergent term, whence the full expressions of the divergent term are used in the implementations of this work.

## 5 Model systems and results

The implementation of the field enhancement calculation presented in Section 4.2 is applied to three different structures. First, in Section 5.1, the time propagation and Casida methods are compared and cross-verified by using linear metal atom chain as a test system. In Section 5.2, a system of two small nearby metal clusters is used to study interaction between plasmon modes of the clusters. Finally, a larger system, a graphene nanoribbon, is studied in Section 5.3.

### 5.1 Linear metal atom chain

Linear metal atom chains have been studied extensively in the literature as a simplest atomistic system that supports localized surface plasmon resonances [28, 29]. The d-electron screening have been observed in a TDDFT study of silver chains [30] and different approaches for analyzing the plasmonic nature of the excitations have been described [29, 32, 33], c.f. discussion of these studies in Section 2.4.

In this work, a linear chain of 14 sodium atoms,  $\text{Na}_{14}$ , is used to test the implementation of the field enhancement calculation in the time propagation and Casida methods, and also to discuss important concepts related to plasmon resonances. All excitations in the atom chain are not discussed here as they are well described in the previous studies [28–30]. Separation between sodium atoms is fixed to 2.89 Å, corresponding to the experimental configuration of atom chains on NiAl(100) surface [103] and used in previous study [29]. The chain was positioned in a rectangular box with 10 Å of vacuum around the chain along all principal directions of the box. Grid-spacing for the spatial discretization was 0.3 Å and spin-paired calculations were performed. Only the 3s-electrons of sodium atoms were explicitly included in the calculations and other electrons were treated as a frozen core. PBE exchange-correlation functional [83] with adiabatic approximation was used. For the time propagation method, the time step was 10 as and propagation time 40 fs. For Casida method, in total 200 Kohn-Sham states were used, 7 lowest of which were doubly occupied by the electrons of the chain. Gaussian spectral broadening with  $\sigma = 0.1$  eV was used. These parameters were observed to ensure the convergence of the excitation energies and strengths within 0.1 eV and 10 %, respectively.

The absorption spectrum  $S(\omega)$  and polarizability spectrum  $\alpha(\omega)$  of the  $\text{Na}_{14}$  chain are shown in Figure 5.1 for longitudinal and transversal perturbations. The spectra calculated with the time propagation and Casida methods agree well as expected [94]. The slightly larger disagreement at higher energies is expected to vanish by further refining simulation parameters.

Figure 5.2 presents comparison of the induced densities at the  $L_0$  excitation between time propagation and Casida method. The agreement between the methods is excellent, providing cross-verification of the implementations. Minor differences in the induced density are expected to vanish by increasing the Kohn-Sham basis size in Casida calculation since attaining all details in real space is expected to require high number of basis functions, c.f. from (4.20) that Casida method presents induced density in a basis formed by pair densities  $\rho_{ij\sigma}(\mathbf{r})$ . Inspection of induced

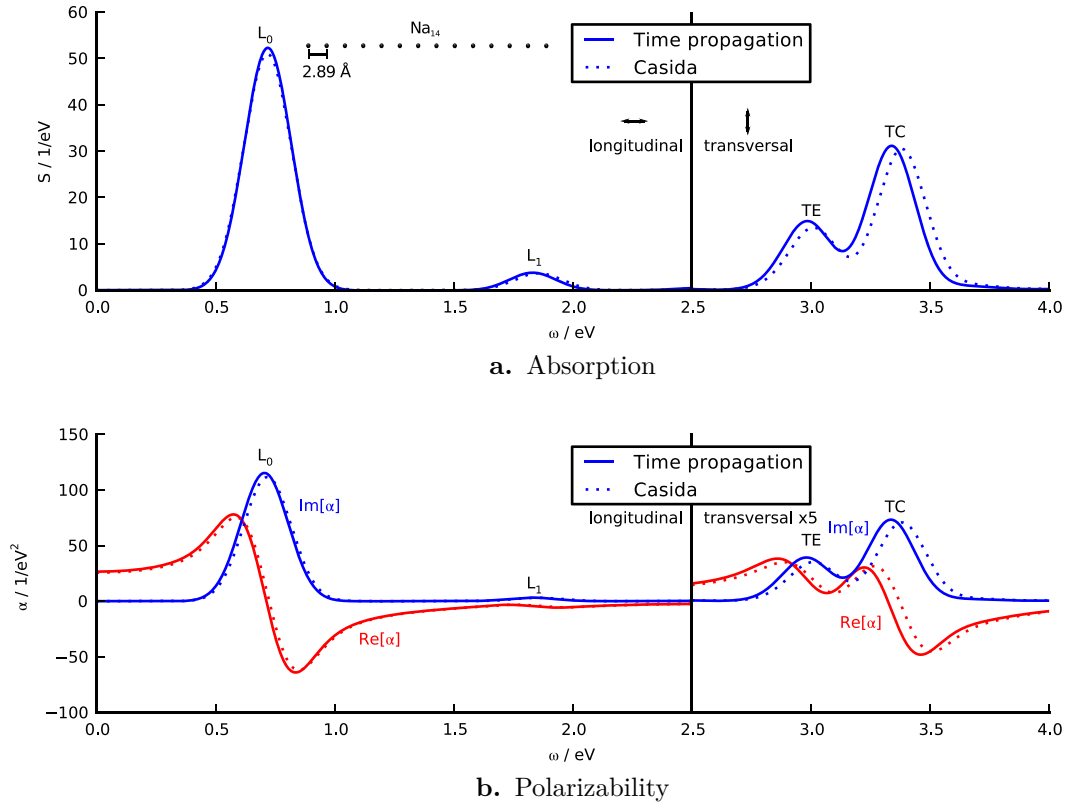


**Figure 5.1.** Photoabsorption and polarizability spectrum of  $\text{Na}_{14}$  chain calculated with time propagation and Casida methods. Transversal polarizability spectrum is multiplied by a factor 5.

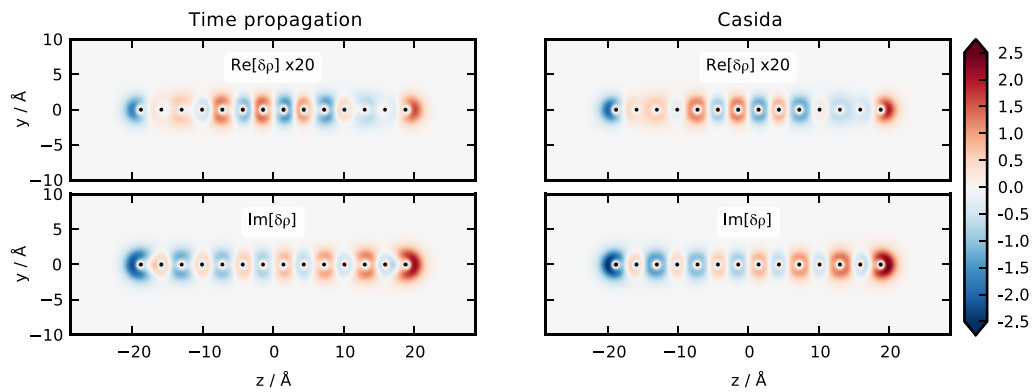


**Figure 5.2.** Induced density at the  $L_0$  excitation on the plane of the chain as calculated with time propagation and Casida methods. Real parts are multiplied by factor 20.

densities at the other excitations,  $L_1$ , TE and TC shows similar agreement between time propagation and Casida methods.

Instead of considering real and imaginary parts of the complex induced density, one can depict the same information by using absolute value and phase. This is exemplified for the TE excitation in Figure 5.3. The imaginary part describes absorption, which justifies the use of plain imaginary part plot in many cases. However, when considering the electric field, both the real and imaginary parts are relevant. At excitation frequencies, the imaginary response is dominant as an integral quantity such as polarizability, c.f. Figure 5.1b, but it might not be dominant over the whole real space. For example, at the TE excitation, the absorption takes place mostly in the ends of the chain as the imaginary part is significant there. However, in the central region of the chain, the real response is dominant in comparison to the imaginary response. Both of these aspects are well realized in the phase plot, although relative strengths of different phase colors remain rather obscure. Additionally, pure imaginary part plot gives rather good intuitive view of the excitation and is more convenient than the phase plot due to its use in existing literature.

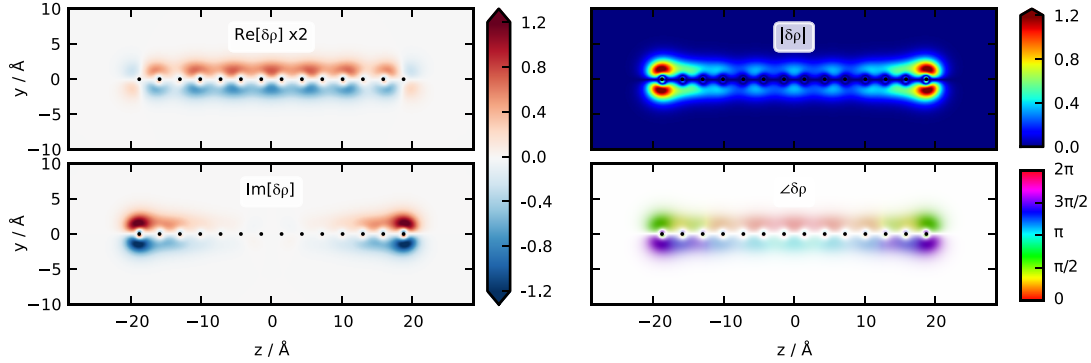


**Figure 5.3.** Induced density at the TE excitation presented both in terms of real and imaginary parts and absolute value and complex phase.

From the induced density  $\delta\rho$  calculated with either time propagation or Casida method, the induced electric potential,  $\delta\phi$ , the induced electric near field  $\delta\mathbf{E}$  and finally the field enhancement FE are calculated as described in Section 4.2. This procedure is illustrated in Figure 5.4 for the  $L_0$  excitation. One should note that  $\delta\rho$ ,  $\delta\phi$  and  $\delta\mathbf{E}$  are complex quantities and both real and imaginary parts are required to properly calculate the field enhancement. However, for visual convenience, only imaginary parts of these quantities are shown in Figure 5.4. Additionally, in the case of the  $L_0$  excitation, the real parts are vanishing, c.f. Figure 5.2, meaning that the  $L_0$  excitation consists of pure out-of-phase oscillation of electrons.

Although the strongest plasmon response is observed at the resonance frequency, the field enhancement resulting from the charge density oscillation at smaller frequencies is not negligible. Below the resonance frequency, the electron density oscillates in the phase of the external field and the response is purely real in frequency space, c.f. longitudinal polarizability at  $\omega < 0.4$  eV in Figure 5.1b. The induced density and the field enhancement in this regime are shown in Figure 5.5. The real

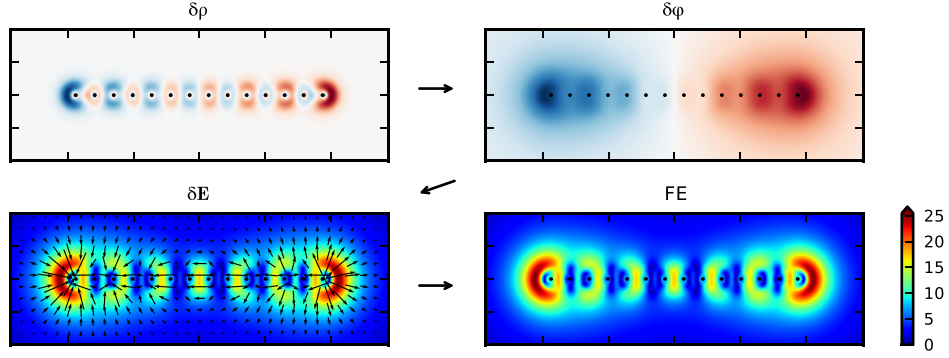


**Figure 5.4.** Illustration of calculation procedure from induced density to field enhancement for the  $L_0$  excitation.

part of induced density looks the same as the imaginary part at the resonance, c.f. Figure 5.2, since the real part can be thought as a "tail" of the  $L_0$  plasmon resonance: the only difference between real and imaginary parts is the prefactor in (4.30) or (4.33) due to Kramers-Kronig relations, i.e. due to causality. Only the magnitude of electron density oscillations is different, as can also be expected from the polarizability spectrum. Analogously, the rather strong real response in the center of the chain at the TE excitation, c.f. Figure 5.3, can be understood to originate from the "tail" of the close TC excitation. Similarly, the "tail" of the TE excitation can be seen in the real part of the induced density at the TC excitation frequency (not shown).

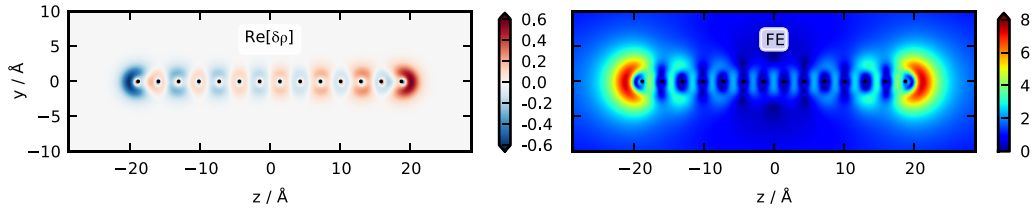


**Figure 5.5.** Induced density and field enhancement for longitudinal perturbation at frequency  $\omega = 0.01$  eV. Imaginary part of induced density is vanishing and thus not shown.

The effect of different PAW corrections, c.f. Section 4.2, to the induced density and field enhancements is shown in Figure 5.6. The all-electron corrections exhibit intensive oscillations near nuclei and clearly the grid shown in Figure 5.6 is not fine enough to correctly describe these oscillations. The compensation charges yield much smoother induced density around atom cores, providing a clear benefit in comparison to the all-electron corrections. The pseudo density is also shown for reference. The field enhancement calculated from the induced density shows similar characteristics as the induced density. In addition, the effect of PAW corrections to the field outside the chain appears to be quite small. At the peak value at  $z \approx \pm 21$  Å the field enhancement calculated from pseudo density differs only by 2 % from the PAW corrected field enhancement. In general, it is not expected that the pseudo

electric field would differ qualitatively from the true field outside the structure but the values may be shifted off from the PAW corrected field by some amount depending on the system.

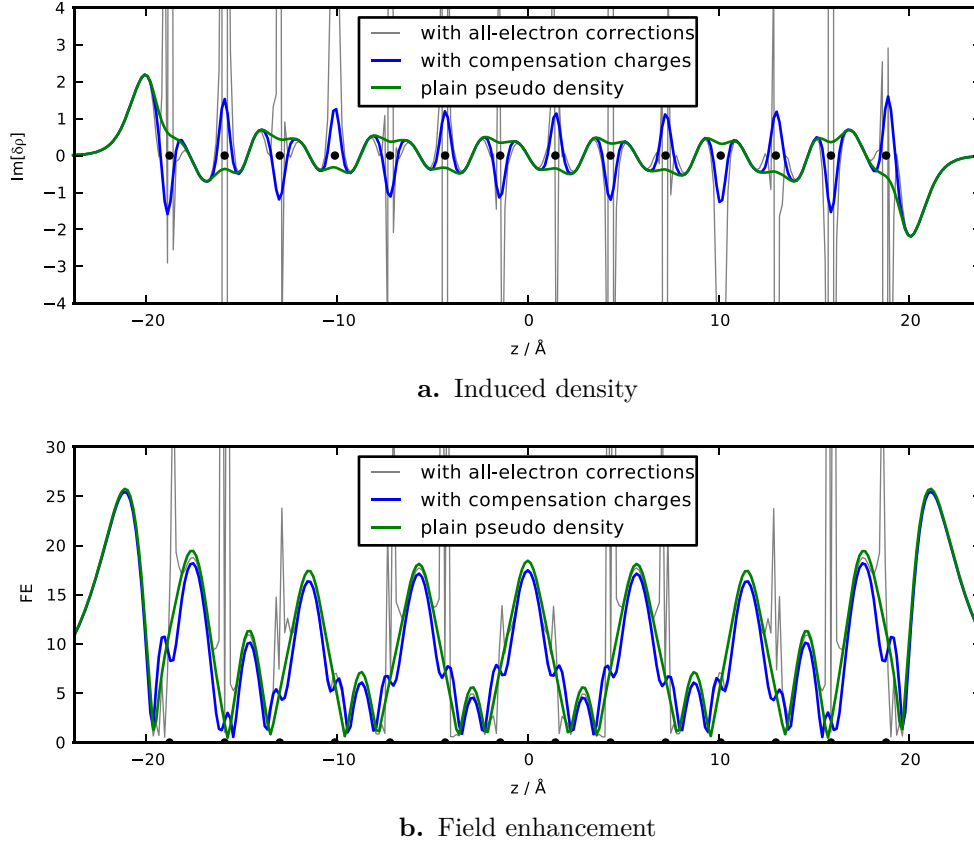


**Figure 5.6.** Induced density and field enhancement at the  $L_0$  excitation along the axis of the chain.

## 5.2 Metal cluster dimer

The strong electric near field resulting from plasmon resonances in a single metal cluster is further magnified when multiple clusters are electrostatically coupled to each other. This coupling is predicted by classical calculations and explained by plasmon hybridization model [17] discussed in Section 2.4. However, when clusters are nearly-touching, the classical description fails as it is not able to describe the molecular bonding and electron tunneling between the clusters. [35,37]

In this section, small clusters are used to study this phenomenon. Clusters consist of 14 sodium atoms in face-centered cubic geometry in  $4 \text{ \AA} \times 4 \text{ \AA} \times 4 \text{ \AA}$  cube. The geometry is illustrated in Figure 5.7b. Cluster geometry is not optimized but rather it serves as a well-defined geometry for studying plasmon resonances. Static properties of similar silver clusters have been studied in the literature and static polarizability has been observed to have a maximum at a specific cluster separation [104,105]. However, silver clusters are not considered in this work as the



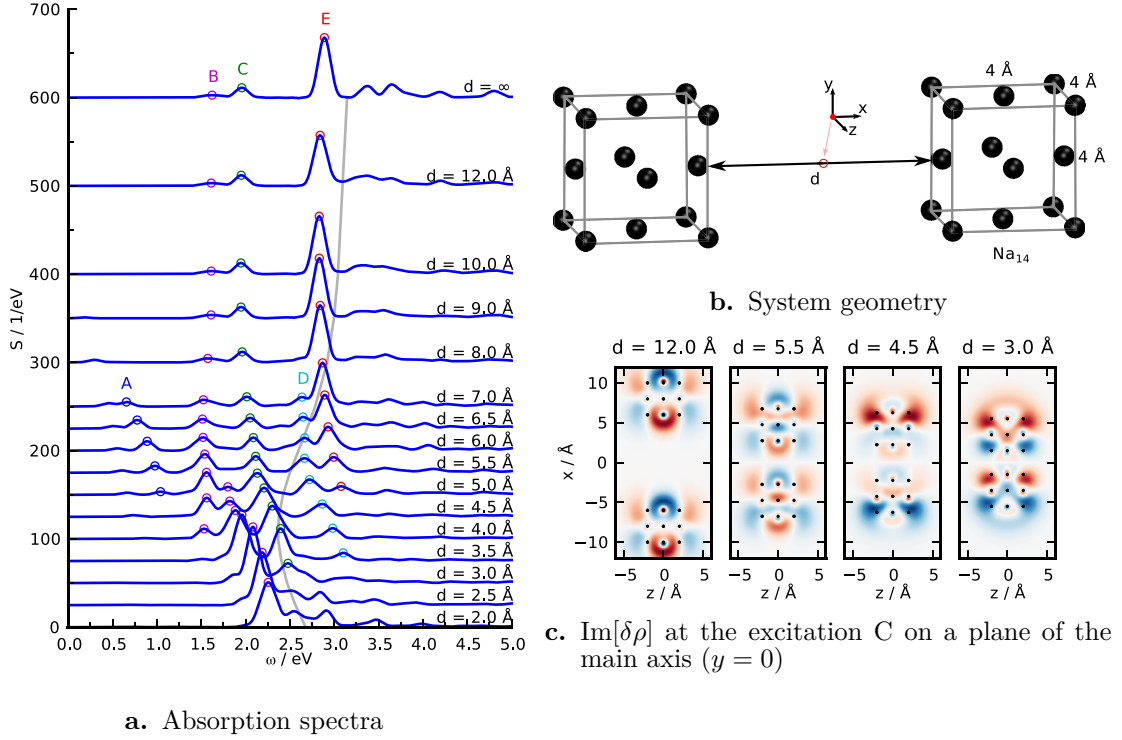


**Figure 5.7.** Development of excitations in cluster dimer with decreasing separation.

focus is on plasmon resonances, which are well captured in simpler sodium clusters. The d-electrons in silver screens the electron gas formed by the s-electrons, and overall, lead to more complicated response of the cluster, which might make the interesting plasmonic behavior harder to observe. On the other hand, sodium has only s-electrons in the valence so it can be used to study general plasmonic properties of the system as the plasmon resonances take place in the electron gas formed by the s-electrons.

Time propagation method is used with similar calculation parameters than those used in Section 5.1 for  $\text{Na}_{14}$  chain with the modification that vacuum size was  $8 \text{ \AA}$  around the clusters and Gaussian spectral broadening was  $\sigma = 0.07 \text{ eV}$  to obtain better distinction between different excitations. The perturbing electric field is aligned along the dimer's principal axis, i.e.  $x$  axis.

Figure 5.7a shows absorption spectra for clusters with decreasing distance  $d$ . The main features of the spectrum remain unchanged down to  $d = 8 \text{ \AA}$ . However, the excitation energies slightly red shift to smaller energies as intercluster distance decreases. Below  $d = 8 \text{ \AA}$ , the tunneling between clusters becomes possible, and below  $d = 5 \text{ \AA}$ , chemical bonding between clusters starts to take place. At such small cluster separations, absorption spectrum undergoes significant changes. Excitation energies start to blue shift to higher energies and the single-cluster excitations change their character significantly (B, C) or completely disappear (E). Additionally, new excitations (A, D) appear in the spectrum.

The general red shift of the excitations for distant clusters can be accounted to be due to classical electrostatic coupling between the clusters and the resulting

hybridization of the plasmon resonances. [106] In the present case, the electrostatic coupling is very small due to the small size of the clusters. Nevertheless, a faint red shift of the main of the main excitation is observable in the absorption spectrum.

The blue shift of the excitation energies have also been observed classically for overlapping dimers. As the clusters penetrate into each other, the dimer can be described as a single cluster with decreasing aspect ratio, where the blue shift of plasmon resonances is a classical effect. [36, 106] For the molecular sized clusters considered here, the increasing quantum confinement is also likely to cause the blue shift.

However, classical description of material with abrupt boundaries is not able to describe the transition from non-contacting to overlapping clusters. Quantum mechanics is required to describe clusters in close contact when the electron tunneling between clusters is possible. Although the response of the system significantly changes when the clusters are brought together, all changes take place continuously. This is illustrated for the excitation C in Figure 5.7c, which presents induced density at the excitation frequency at different cluster separations. The nodal structure of the induced density is roughly the same at all separations but the relative strength of the different antinodes significantly changes. Similarly one can inspect other excitations to verify that they are related. However, although there are clear paths for the excitations A–E marked in Figure 5.7a, different excitations mix as the cluster separation decreases. This happens especially for the excitation B for  $d$  in  $5 \text{ \AA} \dots 4 \text{ \AA}$  as also indicated in the figure by multiple markers.

Previously, Zuloaga *et al.* [35] have studied similar dimer system of spherical metal clusters of diameter  $25 \text{ \AA}$ , treated with the jellium approximation. Instead of multiple excitations observed in Figure 5.7a, in these jellium clusters there is only one main excitation visible. The extra features in the spectrum of  $\text{Na}_{14}$  clusters are expected to originate from the atomistic details of the clusters, which are not present in the jellium approximation. Additionally, the clusters studied in this work are much smaller than those studied by Zuloaga *et al.*, and also the quantum confinement could yield more spectral features. When the cluster size is increased, different excitations may merge to single plasmon excitation. Furthermore, Zuloaga *et al.* used larger spectral broadening, which effectively leads to mixing of close excitations. Nevertheless, the results of the  $\text{Na}_{14}$  clusters and the larger jellium clusters agree qualitatively as similar red and blue shifts at different separations were also observed by Zuloaga *et al.* In addition, by taking weighted average of absorption spectrum over  $0 \text{ eV} \dots 5 \text{ eV}$  for each cluster separation, a rough combined view on the overall response behavior of the dimer can be obtained. The line obtained by this averaging is shown as grey line on the background of Figure 5.7a. This line replicates well the red and blue shifts observed in the large jellium clusters.

The new excitation modes appearing in the absorption spectrum at small distances may have very different characteristics than the excitations that origin from the single cluster. This is exemplified by comparing the excitations A and E in Figure 5.8a. By inspecting the induced density, the excitation E is observed to originate from single-cluster excitations that are similar in both clusters. Instead, the excitation A necessitates the presence of both clusters and, roughly speaking, it is

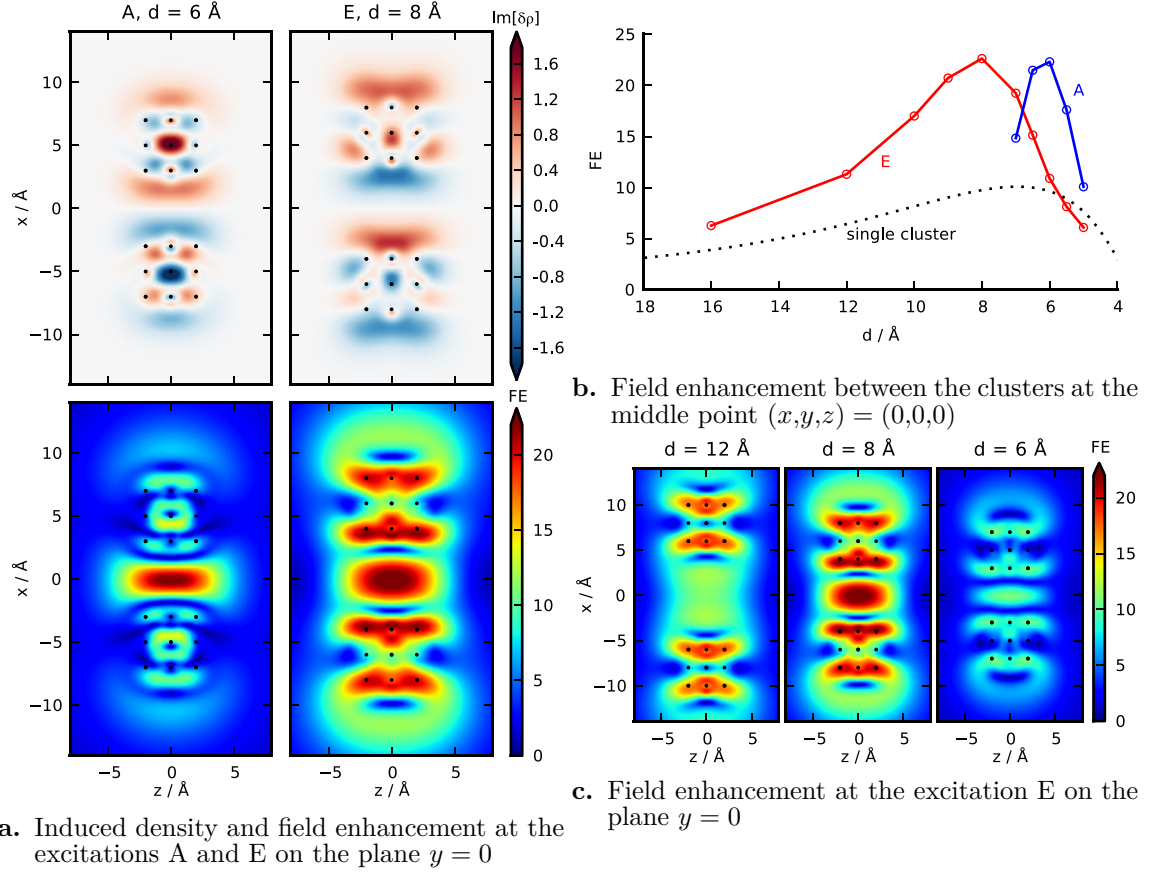


**Figure 5.8.** Behaviour of the hot spot excitations in the sodium cluster dimer.

a dipole oscillation where, by turns, one cluster acts as a positive charge and the other one as a negative charge.

As the excitation E consists of coupled single-cluster plasmon resonances, which have dipolar character, it is also observed in single-cluster photoabsorption spectrum, c.f. Figure 5.7a. Contrary to this, at the excitation A, the charge density oscillation over individual clusters is of higher multipolar order, whence its single-particle counterpart do not couple to light. However, with the Casida method also those excitations which have zero dipole moment can be studied. In fact, the single cluster exhibit an excitation whose transition density is similar to charge density oscillations in both clusters at the excitation A. Thus, the excitation A can be interpreted as electron tunneling mediated plasmon resonance, consisting of two quadrupolar plasmon resonances which become optically active when hybridized.

These plasmon resonances of different origin could be differentiated by their charge transfer character. This can be estimated by defining charge density balance function

$$\Delta\rho_B(x, \omega) = \int d\mathbf{r}' \theta(x - x') \delta\rho(\mathbf{r}', \omega) = \int_{-\infty}^x dx' \int_{-\infty}^{\infty} dy' \int_{-\infty}^{\infty} dz' \delta\rho(\mathbf{r}', \omega), \quad (5.1)$$

where the choice of axis is specific for the present system. This function is shown for imaginary part of induced density for all discussed excitations at different clus-

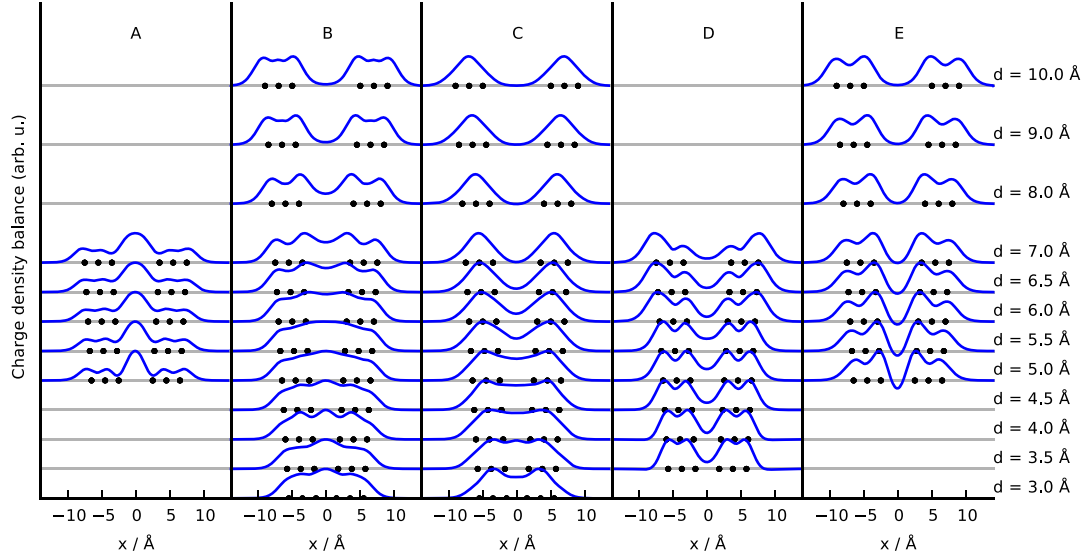
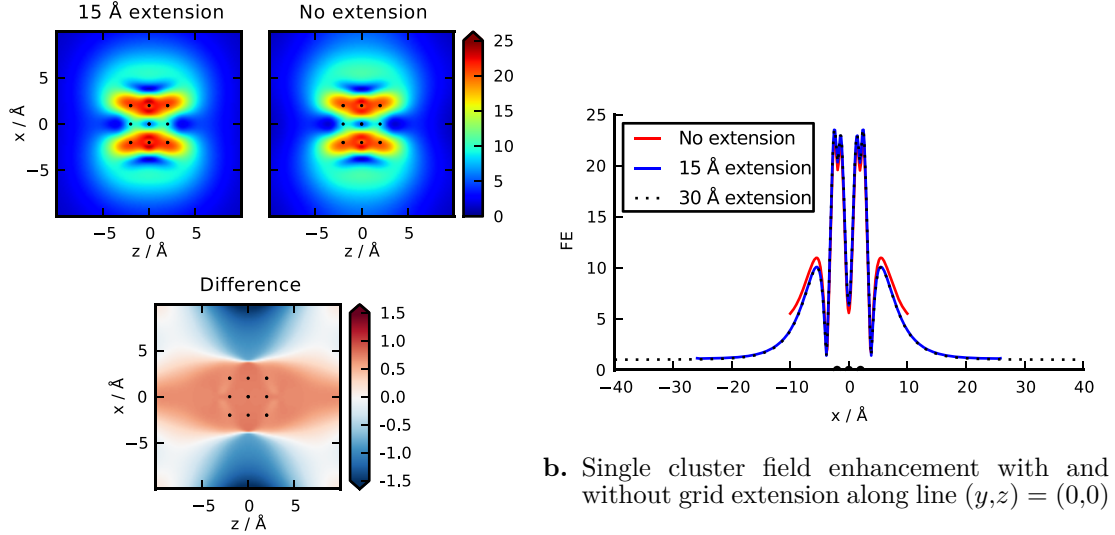


**Figure 5.9.** Charge density balances of the excitations A–E at different cluster separations. Values are scaled to same range for visual convenience.

ter separations in Figure 5.9. By observing density balance between the clusters ( $x = 0$ ), one can observe that for the E excitation, the values are roughly zero, meaning that the charge transfer between clusters is negligible, i.e. dipolar plasmons in both clusters remain neutral. Case is similar for the D excitation. In contrary, for the A excitation the value is largely non-zero at  $x = 0$ , corresponding to significant charge transfer between excitations as expected. For the B and C excitations, the charge transfer character gradually increases as the cluster separation decreases. Zuloaga *et al.* have analyzed the increasing charge transfer character by examining the Kohn-Sham potential between clusters: as the clusters are brought closer, potential barrier between clusters gets narrower and smaller, whence more conducting channels between clusters become available [35].

In spite of the different excitation behavior, both the A and E excitations create a field enhancement hot spot between the clusters as is seen in Figure 5.8a. The field enhancement at the middle point between the clusters is shown in Figure 5.8b in decreasing cluster separation  $d$  for these excitations. The field enhancement at the equivalent distance from a single  $\text{Na}_{14}$  cluster is presented for a reference. Figure shows that the electric near field resulting from two nearby clusters is strongly amplified in comparison to the individual cluster. It is interesting to note that the charge transfer excitation A results in equally large field enhancement values as the conventional coupled plasmon resonance E.

However, when the clusters get closer, the chemical bonding between clusters starts to dim the strong electric field and eventually causes both the A and E excitations to vanish, c.f. Figure 5.7a. This is contrary to classical calculations, which predict extremely strong fields at small distances due to missing charge transfer between clusters. A full real space view of the field enhancement at different cluster separations is shown in Figure 5.8c for the E excitation. These results for the E



a. Single cluster field enhancement with and without grid extension on the plane  $y = 0$

b. Single cluster field enhancement with and without grid extension along line  $(y,z) = (0,0)$

**Figure 5.10.** Effect of the grid extension to resulting field.

excitation closely resemble those observed by Zuloaga *et al.* for larger clusters [35]. However, in their study, only single plasmon resonance is present, and separate plasmon resonance similar to the A excitation is missing, as discussed earlier.

As a technical note regarding to the electric near field calculation, consider Figure 5.10. As discussed in Section 4.2, the simulation grid used for calculating the induced density is extended by adding more vacuum before calculating the induced electric potential to make zero boundary conditions in GPAW's Poisson solver more valid. Figure 5.10a shows field enhancement of a single cluster at the excitation  $E$  when the potential and field are calculated on the original grid and when they are calculated on a grid with 15 Å more vacuum along each positive and negative axis. One can note that if the grid is not extended, the field will have slightly distorted shape, which is especially clear by inspecting the difference of the fields. Further extending the grid does not lead to observable change in the field as depicted by Figure 5.10b. It should be noted that photoabsorption spectrum calculation is not as sensitive to boundary conditions because it depends only on the density that tends to zero faster at the simulation grid boundaries than the electric potential. The converged spectrum is obtained already with the original non-extended grid.

### 5.3 Graphene nanoribbon

As a two dimensional material with unique electronic structure, graphene has many interesting properties in comparison to traditional materials. [107] A graphene sheet of finite width, i.e. graphene nanoribbon, is a promising candidate for semiconducting devices, [108] and atomically well defined graphene nanoribbons have been shown to be experimentally producible. [109] Also the field enhancement phenomenon has been demonstrated in graphene nanoribbons and other graphene flakes. [42, 43] In

this section, the implemented calculation method is used to study field enhancement in a short graphene nanoribbon.

The studied graphene nanoribbon with 206 carbon and 64 hydrogen atoms is shown in Figure 5.11b. Adiabatic PBE exchange-correlation is used and graphene nanoribbon is placed in an orthorhombic box with at least 8 Å vacuum around the ribbon in each direction. Grid spacing of 0.3 Å is used and time propagation scheme with total propagation time of 20 fs, time step of 10 as and Gaussian spectral broadening of  $\sigma = 0.1$  eV is employed.

Figure 5.11a shows absorption spectrum of the graphene nanoribbon when the external electric field is directed along the main axis of the ribbon, i.e.  $x$  axis. To limit the length of the discussion, only the main excitation labeled  $L_0$  is further considered. Figure 5.12 shows the field enhancement at the  $L_0$  excitation. For other excitations in the absorption spectrum, the electric field profiles are similar.

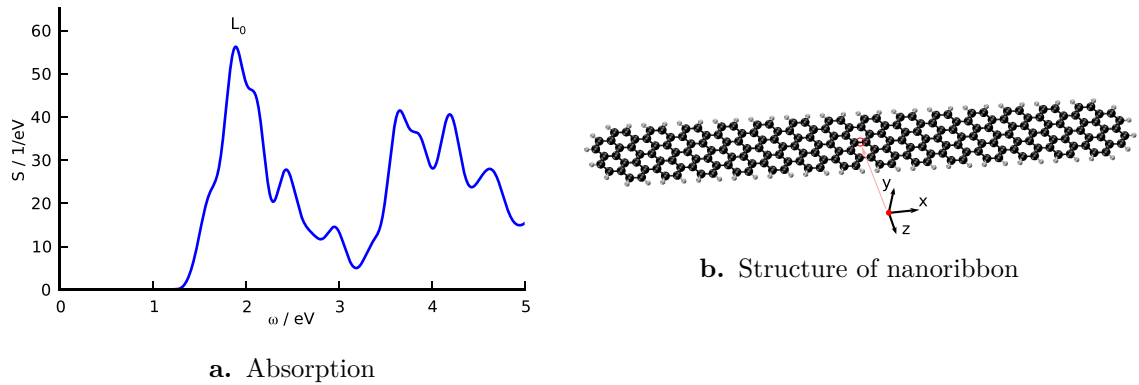


**Figure 5.11.** Absorption spectrum and the studied nanoribbon.

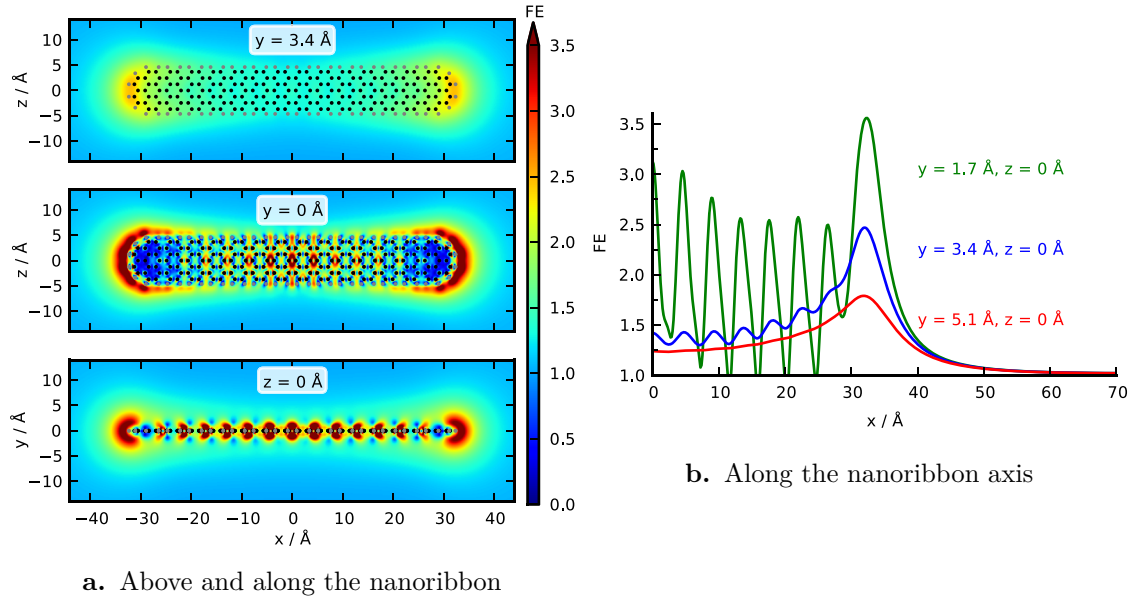


**Figure 5.12.** Field enhancement of the graphene nanoribbon at the  $L_0$  excitation

Previously, Cocchi *et al.* [42] have studied similar graphene nanoribbons with a semi-empirical Hartree-Fock based method. The absorption spectrum obtained with TDDFT in this work shows more features than the spectrum presented by Cocchi *et al.* This is probably due to the differences of the methods, in particular the localized atomic orbital basis used by Cocchi *et al.* However, the field enhancements obtained for the main excitation are similar. Both the spatial distribution of the field and the values are in agreement. To see the quantitative agreement, one needs to consider the different spectral broadening used by Cocchi *et al.*

Namely, at the excitation energy, the imaginary part of the induced field is dominant. Thus, by e.g. (4.20), (4.30) and (4.33), at the excitation energy the induced density scales as  $\delta\rho \propto 1/\eta$  or  $\delta\rho \propto 1/\sigma$  for Lorentzian or Gaussian broadening, respectively, if there are no other excitations close to the excitation in consideration. The induced electric field is linearly related to the induced density so it scales similarly in broadening parameter. In the limit that the induced field is much larger than the external field, the field enhancement is proportional to the induced field, and hence as a quick estimate field enhancement scales as  $\text{FE} \propto 1/\eta$  ( $1/\sigma$ ). This scaling explains the quantitative differences between Figure 5.12 and the study of Cocchi *et al.* [42, Fig. 4] In their study, Cocchi *et al.* have used  $\eta = 0.025$  eV, whereas in this work broadening of 0.1 eV was used. Thus, by multiplying values in Figure 5.12 by a factor  $0.1/0.025 = 4$  one obtains a quantitative agreement with the values presented by Cocchi *et al.*

As the graphene nanoribbon has non-metallic electronic structure, the observed field enhancement values are modest in comparison to those observed in smaller metal clusters in Sections 5.1 and 5.2. Nevertheless, the field enhancement is not negligible, which may allow applicability of graphene nanoribbons in novel contexts.

## 6 Conclusions

Localized surface plasmon resonances in metallic nanoparticles have unique optical properties that have found their use in technological applications as well as have resulted in observation of new interesting phenomena. The development of nanofabrication techniques have made the quantum regime accessible in experimental studies, whence the quantum mechanical first principles understanding of plasmon resonances is becoming increasingly important.

In this work, a quantum mechanical method, time-dependent density functional theory (TDDFT), was used to simulate plasmon resonances in small molecular scale systems. The main part of the work consisted of implementing calculation methods for analyzing plasmonic charge density oscillations and the associated electric near field enhancements. The implementation was done in the GPAW code, which heavily relies on the projector augmented wave (PAW) method. Consequently, the PAW method was reviewed with the emphasis on the parts that were needed in the implementation. Both all-electron and compensation charge corrections were implemented and their contribution to the induced electric field was studied.

The linear response theory for optical properties was reviewed starting from the many-body Schrödinger equation. The formal justification of mapping the description in terms of many-body wave function to the time-dependent electron density, i.e. time-dependent density functional theory, was also presented. Also practical schemes of TDDFT both in real time and in frequency space were reviewed. The induced density and field enhancement calculation methods were implemented both in real time and frequency space. The  $\delta$ -pulse perturbation scheme was employed in the real time implementation. This scheme allows the study of all plasmon resonances in single time propagation, which is a great advantage over the approaches using perturbation at fixed frequency. For frequency space implementation, Casida formulation was used. In this approach, the induced density and field enhancement calculations becomes just a single post-processing step. All in all, the implemented methods are built over the standard TDDFT calculations and their extra computational cost is minor. Thus, the additional information they provide make their use in any TDDFT calculation advantageous.

The methods implemented in this work were tested by utilizing them for several molecular systems. A direct comparison between real time and frequency space implementations was presented, and excellent agreement was demonstrated for linear sodium atom chain. Molecular sodium cluster dimer was also studied. The results were compared to previously published classical studies and quantum mechanical jellium studies. The essential features of plasmon resonances, as well as the quantum effects observed in larger jellium clusters, were reproduced also by this molecular system. Furthermore, the methods implemented in this work enable atomistic modeling of plasmon resonances, and effects from the molecular size and exact atomic structure were also observed in the cluster dimer. The atomistic effects can also be important in larger clusters. For example, the atomistic modeling is required to get accurate description of the surface. In addition, accurate description of atom-wise localized features, such as d-electrons in noble metal atoms, necessitates atomistic



modeling instead of the simple jellium approximation.

The atomistic modeling is also required for systems that do not have free-electron-metal-like electronic structure. As an example of such system, a graphene nanoribbon was also studied. For its most prominent optical excitation, the calculated field enhancement showed good agreement with a previous study from the literature.

However, the methodology of the present work has its limitations. First of all, one should be aware of the limitations of the used theory level, starting from the Born-Oppenheimer approximation, treatment of the perturbing field classically in dipole approximation and imperfect description of many-body effects in terms of adiabatic exchange-correlation functional in TDDFT. Nevertheless, with these standard assumptions, TDDFT has been shown to be good approach for studying optical properties of molecules and small clusters. The methods implemented in this work are in line with the other assumptions: the induced electric field is treated classically and in the quasi-static limit, which is justified for small structures. Correspondingly, the implemented methods are limited only to finite sized systems. In addition, the effect of the environment to the observed optical properties should be addressed. For example, if the molecular system is positioned on a substrate, the coupling between the system and substrate may strongly alter the observed properties.

To conclude, this work provides useful tools for studying quantum plasmon resonances in nanostructures with full atomistic background potential. The tools can be also used to analyze any excitation in a molecule. Furthermore, the program code is open source and freely available in the GPAW repository. The results shown in this work pave the way for understanding plasmon resonances in molecular scale and the implemented methods provide access to atomistic quantum effects also in larger systems.

## References

- [1] L. Hunt, *The true story of Purple of Cassius*, Gold Bulletin **9**, 134 (1976). doi:10.1007/BF03215423.
- [2] M. Faraday, *The Bakerian Lecture: Experimental Relations of Gold (and Other Metals) to Light*, Philosophical Transactions of the Royal Society of London **147**, 145 (1857). doi:10.1098/rstl.1857.0011.
- [3] J. C. Maxwell, *A Dynamical Theory of the Electromagnetic Field*, Philosophical Transactions of the Royal Society of London **155**, 459 (1865). doi:10.1098/rstl.1865.0008.
- [4] G. Mie, *Beiträge zur Optik trüber Medien, speziell kolloidaler Metallösungen*, Annalen der Physik **330**, 377 (1908). doi:10.1002/andp.19083300302.
- [5] R. Gans, *Über die Form ultramikroskopischer Goldteilchen*, Annalen der Physik **342**, 881 (1912). doi:10.1002/andp.19123420503.
- [6] R. Gans, *Über die Form ultramikroskopischer Silberteilchen*, Annalen der Physik **352**, 270 (1915). doi:10.1002/andp.19153521006.
- [7] N. J. Halas, S. Lal, W.-S. Chang, S. Link, and P. Nordlander, *Plasmons in strongly coupled metallic nanostructures*, Chemical Reviews **111**, 3913 (2011). doi:10.1021/cr200061k.
- [8] S. M. Morton, D. W. Silverstein, and L. Jensen, *Theoretical studies of plasmonics using electronic structure methods*, Chemical Reviews **111**, 3962 (2011). doi:10.1021/cr100265f.
- [9] V. Giannini, A. I. Fernández-Domínguez, S. C. Heck, and S. A. Maier, *Plasmonic nanoantennas: Fundamentals and their use in controlling the radiative properties of nanoemitters*, Chemical Reviews **111**, 3888 (2011). doi:10.1021/cr1002672.
- [10] M. Fleischmann, P. Hendra, and A. McQuillan, *Raman spectra of pyridine adsorbed at a silver electrode*, Chemical Physics Letters **26**, 163 (1974). doi:10.1016/0009-2614(74)85388-1.
- [11] D. L. Jeanmaire and R. P. V. Duyne, *Surface Raman spectroelectrochemistry: Part I. Heterocyclic, aromatic, and aliphatic amines adsorbed on the anodized silver electrode*, Journal of Electroanalytical Chemistry and Interfacial Electrochemistry **84**, 1 (1977). doi:10.1016/S0022-0728(77)80224-6.
- [12] M. G. Albrecht and J. A. Creighton, *Anomalous intense Raman spectra of pyridine at a silver electrode*, Journal of the American Chemical Society **99**, 5215 (1977). doi:10.1021/ja00457a071.

- [13] S. Nie and S. R. Emory, *Probing single molecules and single nanoparticles by surface-enhanced Raman scattering*, Science **275**, 1102 (1997). doi:10.1126/science.275.5303.1102.
- [14] K. Kneipp, Y. Wang, H. Kneipp, L. T. Perelman, I. Itzkan, R. R. Dasari, and M. S. Feld, *Single molecule detection using surface-enhanced Raman scattering (SERS)*, Physical Review Letters **78**, 1667 (1997). doi:10.1103/PhysRevLett.78.1667.
- [15] S. A. Maier, P. G. Kik, H. A. Atwater, S. Meltzer, E. Harel, B. E. Koel, and A. A. G. Requicha, *Local detection of electromagnetic energy transport below the diffraction limit in metal nanoparticle plasmon waveguides*, Nature Materials **2**, 229 (2003). doi:10.1038/nmat852.
- [16] E. Prodan, C. Radloff, N. J. Halas, and P. Nordlander, *A hybridization model for the plasmon response of complex nanostructures*, Science **302**, 419 (2003). doi:10.1126/science.1089171.
- [17] P. Nordlander, C. Oubre, E. Prodan, K. Li, and M. I. Stockman, *Plasmon hybridization in nanoparticle dimers*, Nano Letters **4**, 899 (2004). doi:10.1021/nl049681c.
- [18] H. A. Atwater and A. Polman, *Plasmonics for improved photovoltaic devices*, Nature Materials **9**, 205 (2010). doi:10.1038/nmat2629.
- [19] X. Huang, I. H. El-Sayed, W. Qian, and M. A. El-Sayed, *Cancer cell imaging and photothermal therapy in the near-infrared region by using gold nanorods*, Journal of the American Chemical Society **128**, 2115 (2006). doi:10.1021/ja057254a.
- [20] O. Neumann, A. S. Urban, J. Day, S. Lal, P. Nordlander, and N. J. Halas, *Solar vapor generation enabled by nanoparticles*, ACS Nano **7**, 42 (2013). doi:10.1021/nn304948h.
- [21] M. Pelton, J. Aizpurua, and G. Bryant, *Metal-nanoparticle plasmonics*, Laser & Photonics Reviews **2**, 136 (2008). doi:10.1002/lpor.200810003.
- [22] W. Ekardt, *Dynamical polarizability of small metal particles: Self-consistent spherical jellium background model*, Physical Review Letters **52**, 1925 (1984). doi:10.1103/PhysRevLett.52.1925.
- [23] M. J. Puska, R. M. Nieminen, and M. Manninen, *Electronic polarizability of small metal spheres*, Physical Review B **31**, 3486 (1985). doi:10.1103/PhysRevB.31.3486.
- [24] A. Rubio and L. Serra, *Dielectric screening effects on the photoabsorption cross section of embedded metallic clusters*, Physical Review B **48**, 18222 (1993). doi:10.1103/PhysRevB.48.18222.

- [25] A. Rubio, J. A. Alonso, X. Blase, L. C. Balbás, and S. G. Louie, *Ab initio photoabsorption spectra and structures of small semiconductor and metal clusters*, Physical Review Letters **77**, 247 (1996). doi:10.1103/PhysRevLett.77.247.
- [26] I. Vasiliev, S. Ögüt, and J. R. Chelikowsky, *Ab initio excitation spectra and collective electronic response in atoms and clusters*, Physical Review Letters **82**, 1919 (1999). doi:10.1103/PhysRevLett.82.1919.
- [27] S. Kümmel, K. Andrae, and P.-G. Reinhard, *Collectivity in the optical response of small metal clusters*, Applied Physics B: Lasers and Optics **73**, 293 (2001). doi:10.1007/s003400100679.
- [28] S. Gao and Z. Yuan, *Emergence of collective plasmon excitation in a confined one-dimensional electron gas*, Physical Review B **72**, 121406 (2005). doi:10.1103/PhysRevB.72.121406.
- [29] J. Yan, Z. Yuan, and S. Gao, *End and central plasmon resonances in linear atomic chains*, Physical Review Letters **98**, 216602 (2007). doi:10.1103/PhysRevLett.98.216602.
- [30] J. Yan and S. Gao, *Plasmon resonances in linear atomic chains: Free-electron behavior and anisotropic screening of  $d$  electrons*, Physical Review B **78**, 235413 (2008). doi:10.1103/PhysRevB.78.235413.
- [31] K.-Y. Lian, P. Salek, M. Jin, and D. Ding, *Density-functional studies of plasmons in small metal clusters*, The Journal of Chemical Physics **130**, 174701 (2009). doi:10.1063/1.3119310.
- [32] S. Bernadotte, F. Evers, and C. R. Jacob, *Plasmons in molecules*, The Journal of Physical Chemistry C **117**, 1863 (2013). doi:10.1021/jp3113073.
- [33] T. Yasuike, K. Nobusada, and M. Hayashi, *Collectivity of plasmonic excitations in small sodium clusters with ring and linear structures*, Physical Review A **83**, 013201 (2011). doi:10.1103/PhysRevA.83.013201.
- [34] E. Prodan and P. Nordlander, *Structural tunability of the plasmon resonances in metallic nanoshells*, Nano Letters **3**, 543 (2003). doi:10.1021/nl034030m.
- [35] J. Zuloaga, E. Prodan, and P. Nordlander, *Quantum description of the plasmon resonances of a nanoparticle dimer*, Nano Letters **9**, 887 (2009). doi:10.1021/nl803811g.
- [36] J. Zuloaga, E. Prodan, and P. Nordlander, *Quantum plasmonics: Optical properties and tunability of metallic nanorods*, ACS Nano **4**, 5269 (2010). doi:10.1021/nn101589n.
- [37] C. F. A. Negre, E. M. Perassi, E. A. Coronado, and C. G. Sánchez, *Quantum dynamical simulations of local field enhancement in metal nanoparticles*, Journal of Physics: Condensed Matter **25**, 125304 (2013). doi:10.1088/0953-8984/25/12/125304.

- [38] R. Esteban, A. G. Borisov, P. Nordlander, and J. Aizpurua, *Bridging quantum and classical plasmonics with a quantum-corrected model*, Nature Communications **3**, 825 (2012). doi:10.1038/ncomms1806.
- [39] J. M. Pitarke, V. M. Silkin, E. V. Chulkov, and P. M. Echenique, *Theory of surface plasmons and surface-plasmon polaritons*, Reports on Progress in Physics **70**, 1 (2007). doi:10.1088/0034-4885/70/1/R01.
- [40] L. Jensen, C. M. Aikens, and G. C. Schatz, *Electronic structure methods for studying surface-enhanced Raman scattering*, Chemical Society Reviews **37**, 1061 (2008). doi:10.1039/B706023H.
- [41] H. E. Johnson and C. M. Aikens, *Electronic structure and TDDFT optical absorption spectra of silver nanorods*, The Journal of Physical Chemistry A **113**, 4445 (2009). doi:10.1021/jp811075u.
- [42] C. Cocchi, D. Prezzi, A. Ruini, E. Benassi, M. J. Caldas, S. Corni, and E. Molinari, *Optical excitations and field enhancement in short graphene nanoribbons*, The Journal of Physical Chemistry Letters **3**, 924 (2012). doi:10.1021/jz300164p.
- [43] S. Thongrattanasiri and F. J. García de Abajo, *Optical field enhancement by strong plasmon interaction in graphene nanostructures*, Physical Review Letters **110**, 187401 (2013). doi:10.1103/PhysRevLett.110.187401.
- [44] M. A. L. Marques, N. T. Maitra, F. M. S. Nogueira, E. K. U. Gross, and A. Rubio, eds., *Fundamentals of Time-Dependent Density Functional Theory* (Springer, 2012). ISBN 978-3-642-23517-7 (printed). ISBN 978-3-642-23518-4 (electric). doi:10.1007/978-3-642-23518-4.
- [45] R. M. Martin, *Electronic Structure: Basic Theory and Practical Methods* (Cambridge University Press, 2004). ISBN 978-0-521-78285-2.
- [46] M. Born and R. Oppenheimer, *Zur Quantentheorie der Molekeln*, Annalen der Physik **389**, 457 (1927). doi:10.1002/andp.19273892002.
- [47] W. M. C. Foulkes, L. Mitas, R. J. Needs, and G. Rajagopal, *Quantum Monte Carlo simulations of solids*, Reviews of Modern Physics **73**, 33 (2001). doi:10.1103/RevModPhys.73.33.
- [48] A. Szabo and N. S. Ostlund, *Modern Quantum Chemistry: Introduction to Advanced Electronic Structure Theory* (Dover Publications, 1996). ISBN 978-0-486-69186-2.
- [49] M. O. Scully and M. S. Zubairy, *Quantum optics* (Cambridge University Press, 1997). ISBN 978-0-521-43458-4.
- [50] A. L. Fetter and J. D. Walecka, *Quantum Theory of Many-Particle Systems* (McGraw-Hill, 1971). ISBN 978-0-07-020653-3.

- [51] M. E. Casida, *Time-dependent density functional response theory for molecules*, in *Recent Advances in Density Functional Methods, Part I*, edited by D. P. Chong (World Scientific, Singapore, 1995), p. 155. doi:10.1142/9789812830586\_0005.
- [52] G. Onida, L. Reining, and A. Rubio, *Electronic excitations: density-functional versus many-body Green's-function approaches*, Reviews of Modern Physics **74**, 601 (2002). doi:10.1103/RevModPhys.74.601.
- [53] A. D. McLachlan and M. A. Ball, *Time-dependent Hartree-Fock theory for molecules*, Reviews of Modern Physics **36**, 844 (1964). doi:10.1103/RevModPhys.36.844.
- [54] S. R. Elliott, *The Physics and Chemistry of Solids* (John Wiley & Sons, 1998). ISBN 978-0-471-98195-4.
- [55] N. W. Ashcroft and N. D. Mermin, *Solid State Physics* (Saunders College Publishing, 1976). ISBN 978-0-03-083993-1.
- [56] S. Svanberg, *Atomic and Molecular Spectroscopy* (Springer Berlin Heidelberg, 2004). ISBN 978-3-540-20382-7 (printed). ISBN 978-3-642-18520-5 (electric). doi:10.1007/978-3-642-18520-5.
- [57] U. Kreibig and M. Vollmer, *Optical Properties of Metal Clusters* (Springer Berlin Heidelberg, 1995). ISBN 978-3-642-08191-0 (printed). ISBN 978-3-662-09109-8 (electric). doi:10.1007/978-3-662-09109-8.
- [58] A. L. Koh, K. Bao, I. Khan, W. E. Smith, G. Kothleitner, P. Nordlander, S. A. Maier, and D. W. McComb, *Electron energy-loss spectroscopy (EELS) of surface plasmons in single silver nanoparticles and dimers: Influence of beam damage and mapping of dark modes*, ACS Nano **3**, 3015 (2009). doi:10.1021/nn900922z.
- [59] F.-P. Schmidt, H. Ditlbacher, U. Hohenester, A. Hohenau, F. Hofer, and J. R. Krenn, *Dark plasmonic breathing modes in silver nanodisks*, Nano Letters **12**, 5780 (2012). doi:10.1021/nl3030938.
- [60] J. P. Kottmann and O. J. F. Martin, *Retardation-induced plasmon resonances in coupled nanoparticles*, Optics Letters **26**, 1096 (2001). doi:10.1364/OL.26.001096.
- [61] V. R. Manfrinato, L. Zhang, D. Su, H. Duan, R. G. Hobbs, E. A. Stach, and K. K. Berggren, *Resolution limits of electron-beam lithography toward the atomic scale*, Nano Letters **13**, 1555 (2013). doi:10.1021/nl304715p.
- [62] M. Zhu, C. M. Aikens, F. J. Hollander, G. C. Schatz, and R. Jin, *Correlating the crystal structure of a thiol-protected Au<sub>25</sub> cluster and optical properties*, Journal of the American Chemical Society **130**, 5883 (2008). doi:10.1021/ja801173r.

- [63] J. A. Scholl, A. L. Koh, and J. A. Dionne, *Quantum plasmon resonances of individual metallic nanoparticles*, Nature **483**, 421 (2012). doi:10.1038/nature10904.
- [64] J. A. Scholl, A. García-Etxarri, A. L. Koh, and J. A. Dionne, *Observation of quantum tunneling between two plasmonic nanoparticles*, Nano Letters **13**, 564 (2013). doi:10.1021/nl304078v.
- [65] D. M. Eigler and E. K. Schweizer, *Positioning single atoms with a scanning tunnelling microscope*, Nature **344**, 524 (1990). doi:10.1038/344524a0.
- [66] N. Nilius, T. M. Wallis, and W. Ho, *Development of one-dimensional band structure in artificial gold chains*, Science **297**, 1853 (2002). doi:10.1126/science.1075242.
- [67] J. N. Crain and D. T. Pierce, *End states in one-dimensional atom chains*, Science **307**, 703 (2005). doi:10.1126/science.1106911.
- [68] C. Xia, C. Yin, and V. V. Kresin, *Photoabsorption by volume plasmons in metal nanoclusters*, Physical Review Letters **102**, 156802 (2009). doi:10.1103/PhysRevLett.102.156802.
- [69] F. J. García de Abajo, *Optical excitations in electron microscopy*, Reviews of Modern Physics **82**, 209 (2010). doi:10.1103/RevModPhys.82.209.
- [70] M. Kociak and J. García de Abajo, *Nanoscale mapping of plasmons, photons, and excitons*, MRS Bulletin **37**, 39 (2012). doi:10.1557/mrs.2011.335.
- [71] J. Nelayah, M. Kociak, O. Stephan, F. J. Garcia de Abajo, M. Tence, L. Henrard, D. Taverna, I. Pastoriza-Santos, L. M. Liz-Marzan, and C. Colliex, *Mapping surface plasmons on a single metallic nanoparticle*, Nature Physics **3**, 348 (2007). doi:10.1038/nphys575.
- [72] A. Taflove and S. Hagness, *Computational Electrodynamics: The Finite-Difference Time-Domain Method* (Artech House, 2000). ISBN 978-1-58053-076-7.
- [73] L. V. Brown, H. Sobhani, J. B. Lassiter, P. Nordlander, and N. J. Halas, *Heterodimers: Plasmonic properties of mismatched nanoparticle pairs*, ACS Nano **4**, 819 (2010). doi:10.1021/nn9017312.
- [74] N. Verellen, Y. Sonnefraud, H. Sobhani, F. Hao, V. V. Moshchalkov, P. V. Dorpe, P. Nordlander, and S. A. Maier, *Fano resonances in individual coherent plasmonic nanocavities*, Nano Letters **9**, 1663 (2009). doi:10.1021/nl9001876.
- [75] K. J. Savage, M. M. Hawkeye, R. Esteban, A. G. Borisov, J. Aizpurua, and J. J. Baumberg, *Revealing the quantum regime in tunnelling plasmonics*, Nature **491**, 574 (2012). doi:10.1038/nature11653.

- [76] B.-J. Wang, Y. Xu, and S.-H. Ke, *Plasmon excitations in sodium atomic planes: A time-dependent density functional theory study*, The Journal of Chemical Physics **137**, 054101 (2012). doi:10.1063/1.4739952.
- [77] S. A. Maier, *Plasmonics: Fundamentals and Applications* (Springer US, 2007). ISBN 978-0-387-33150-8 (printed). ISBN 978-0-387-37825-1 (electric). doi:10.1007/0-387-37825-1.
- [78] W. L. Barnes, A. Dereux, and T. W. Ebbesen, *Surface plasmon subwavelength optics*, Nature **424**, 824 (2003). doi:10.1038/nature01937.
- [79] H. Raether, *Surface Plasmons on Smooth and Rough Surfaces and on Gratings* (Springer Berlin Heidelberg, 1988). ISBN 978-3-540-17363-2 (printed). ISBN 978-3-540-47441-8 (electric). doi:10.1007/BFb0048317.
- [80] P. Hohenberg and W. Kohn, *Inhomogeneous electron gas*, Physical Review **136**, B864 (1964). doi:10.1103/PhysRev.136.B864.
- [81] U. von Barth and L. Hedin, *A local exchange-correlation potential for the spin polarized case: I*, Journal of Physics C: Solid State Physics **5**, 1629 (1972). doi:10.1088/0022-3719/5/13/012.
- [82] W. Kohn and L. J. Sham, *Self-consistent equations including exchange and correlation effects*, Physical Review **140**, A1133 (1965). doi:10.1103/PhysRev.140.A1133.
- [83] J. P. Perdew, K. Burke, and M. Ernzerhof, *Generalized gradient approximation made simple*, Physical Review Letters **77**, 3865 (1996). doi:10.1103/PhysRevLett.77.3865.
- [84] E. Runge and E. K. U. Gross, *Density-functional theory for time-dependent systems*, Physical Review Letters **52**, 997 (1984). doi:10.1103/PhysRevLett.52.997.
- [85] K. L. Liu and S. H. Vosko, *A time-dependent spin density functional theory for the dynamical spin susceptibility*, Canadian Journal of Physics **67**, 1015 (1989). doi:10.1139/p89-178.
- [86] A. Zangwill and P. Soven, *Density-functional approach to local-field effects in finite systems: Photoabsorption in the rare gases*, Physical Review A **21**, 1561 (1980). doi:10.1103/PhysRevA.21.1561.
- [87] A. Castro, M. A. L. Marques, and A. Rubio, *Propagators for the time-dependent Kohn-Sham equations*, The Journal of Chemical Physics **121**, 3425 (2004). doi:10.1063/1.1774980.
- [88] K. Yabana and G. F. Bertsch, *Time-dependent local-density approximation in real time*, Physical Review B **54**, 4484 (1996). doi:10.1103/PhysRevB.54.4484.



- [89] J. Yan, J. J. Mortensen, K. W. Jacobsen, and K. S. Thygesen, *Linear density response function in the projector augmented wave method: Applications to solids, surfaces, and interfaces*, Physical Review B **83**, 245122 (2011). doi:10.1103/PhysRevB.83.245122.
- [90] M. E. Casida, *Time-dependent density functional response theory of molecular systems: Theory, computational methods, and functionals*, in *Recent Developments and Applications of Modern Density Functional Theory*, edited by J. M. Seminario (Elsevier, Amsterdam, 1996), p. 391. doi:10.1016/S1380-7323(96)80093-8.
- [91] M. A. L. Marques, C. A. Ullrich, F. Nogueira, A. Rubio, K. Burke, and E. K. U. Gross, eds., *Time-Dependent Density Functional Theory* (Springer, 2006). ISBN 978-3-540-35422-2 (printed). ISBN 978-3-540-35426-0 (electric). doi:10.1007/b11767107.
- [92] *Grid-based projector-augmented wave method* (online). <https://wiki.fysik.dtu.dk/gpaw/>.
- [93] J. J. Mortensen, L. B. Hansen, and K. W. Jacobsen, *Real-space grid implementation of the projector augmented wave method*, Physical Review B **71**, 035109 (2005). doi:10.1103/PhysRevB.71.035109.
- [94] M. Walter, H. Häkkinen, L. Lehtovaara, M. Puska, J. Enkovaara, C. Rostgaard, and J. J. Mortensen, *Time-dependent density-functional theory in the projector augmented-wave method*, The Journal of Chemical Physics **128**, 244101 (2008). doi:10.1063/1.2943138.
- [95] J. Enkovaara, C. Rostgaard, J. J. Mortensen, J. Chen, M. Duřak, L. Ferrighi, J. Gavnholt, C. Glinsvad, V. Haikola, H. A. Hansen, H. H. Kristoffersen, M. Kuisma, A. H. Larsen, L. Lehtovaara, M. Ljungberg, O. Lopez-Acevedo, P. G. Moses, J. Ojanen, T. Olsen, V. Petzold, N. A. Romero, J. Stausholm-Møller, M. Strange, G. A. Tritsarlis, M. Vanin, M. Walter, B. Hammer, H. Häkkinen, G. K. H. Madsen, R. M. Nieminen, J. K. Nørskov, M. Puska, T. T. Rantala, J. Schiøtz, K. S. Thygesen, and K. W. Jacobsen, *Electronic structure calculations with GPAW: a real-space implementation of the projector augmented-wave method*, Journal of Physics: Condensed Matter **22**, 253202 (2010). doi:10.1088/0953-8984/22/25/253202.
- [96] *Atomic Simulation Environment* (online). <https://wiki.fysik.dtu.dk/ase/>.
- [97] S. Bahn and K. Jacobsen, *An object-oriented scripting interface to a legacy electronic structure code*, Computing in Science Engineering **4**, 56 (2002). doi:10.1109/5992.998641.
- [98] P. E. Blöchl, *Projector augmented-wave method*, Physical Review B **50**, 17953 (1994). doi:10.1103/PhysRevB.50.17953.

- [99] P. Blöchl, C. Först, and J. Schimpl, *Projector augmented wave method: ab initio molecular dynamics with full wave functions*, Bulletin of Materials Science **26**, 33 (2003). doi:10.1007/BF02712785.
- [100] A. Castro, A. Rubio, and M. J. Stott, *Solution of Poisson's equation for finite systems using plane-wave methods*, Canadian Journal of Physics **81**, 1151 (2003). doi:10.1139/p03-078.
- [101] F. W. King, *Hilbert Transforms, Volume 2* (Cambridge University Press, 2009). ISBN 978-0-521-51720-1 (printed). ISBN 978-0-511-73527-1 (electric). doi:10.1017/CB09780511735271.
- [102] M. Quijada, R. D. Muiño, A. G. Borisov, J. A. Alonso, and P. M. Echenique, *Lifetime of electronic excitations in metal nanoparticles*, New Journal of Physics **12**, 053023 (2010). doi:10.1088/1367-2630/12/5/053023.
- [103] G. V. Nazin, X. H. Qiu, and W. Ho, *Atomic engineering of photon emission with a scanning tunneling microscope*, Physical Review Letters **90**, 216110 (2003). doi:10.1103/PhysRevLett.90.216110.
- [104] K. Zhao, M. C. Tropicovsky, D. Xiao, A. G. Eguiluz, and Z. Zhang, *Electronic coupling and optimal gap size between two metal nanoparticles*, Physical Review Letters **102**, 186804 (2009). doi:10.1103/PhysRevLett.102.186804.
- [105] M. C. Tropicovsky, K. Zhao, D. Xiao, A. G. Eguiluz, and Z. Zhang, *Molecular orbital view of the electronic coupling between two metal nanoparticles*, Physical Review B **82**, 045413 (2010). doi:10.1103/PhysRevB.82.045413.
- [106] J. B. Lassiter, J. Aizpurua, L. I. Hernandez, D. W. Brandl, I. Romero, S. Lal, J. H. Hafner, P. Nordlander, and N. J. Halas, *Close encounters between two nanoshells*, Nano Letters **8**, 1212 (2008). doi:10.1021/nl080271o.
- [107] A. K. Geim, *Graphene: Status and prospects*, Science **324**, 1530 (2009). doi:10.1126/science.1158877.
- [108] M. J. Allen, V. C. Tung, and R. B. Kaner, *Honeycomb carbon: A review of graphene*, Chemical Reviews **110**, 132 (2010). doi:10.1021/cr900070d.
- [109] J. Cai, P. Ruffieux, R. Jaafar, M. Bieri, T. Braun, S. Blankenburg, M. Muoth, A. P. Seitsonen, M. Saleh, X. Feng, K. Mullen, and R. Fasel, *Atomically precise bottom-up fabrication of graphene nanoribbons*, Nature **466**, 470 (2010). doi:10.1038/nature09211.